TUDelft

Delft University of Technology

Effects of repeated hydraulic loads on microstructure and hydraulic behaviour of a compacted clayey silt

Azizi, Arash; Musso, Guido; Jommi, Cristina

Important note
To cite this publication, please use the final published version (if applicable).
Please check the document version above.

1   **Effects of repeated hydraulic loads on microstructure and hydraulic behaviour**

2   **of a compacted clayey silt**

3

4   Arash Azizi[1*], Guido Musso[2] and Cristina Jommi[3, 4]

5

6   *Corresponding author

7   1. Post-doc Researcher

8   Department of Structural, Geotechnical and Building Engineering

9   Politecnico di Torino

10   Corso Duca degli Abruzzi, 24

11   10129 Torino, Italy

12   arash.azizi@polito.it

13   Currently:

14   Research Fellow

15   Department of Engineering

16   Durham University

17   Lower Mountjoy, South Rd.

18   DH1 3LE Durham, UK

19   arash.azizi@durham.ac.uk

20   2. Associate Professor

21   Department of Structural, Geotechnical and Building Engineering

22   Politecnico di Torino

23   Corso Duca degli Abruzzi, 24

24   10129 Torino, Italy

25   guido.musso@polito.it

26   3. Professor

27   Department of Civil and Environmental Engineering,

28   Politecnico di Milano

29   Piazza Leonardo da Vinci, 32

30   20133 Milano, Italy

31   cristina.jommi@polimi.it

32   4. Professor

33   Department of Geosciences and Engineering

34   Delft University of Technology

35   Stevin weg 1

36   2628CN Delft, The Netherlands

37   c.jommi@tudelft.nl

38

Abstract

Soils used in earth constructions are mostly unsaturated, and they undergo frequent drying-wetting cycles (repeated hydraulic loads) due to changes in climatic conditions or variations of the ground water level, particularly at shallow depths. After compaction, changes in water content can significantly influence the hydromechanical response of the construction material, which therefore has to be assessed for repeated hydraulic loads. This research investigates the effect of such loads on the microstructure and hydraulic behaviour of a silty soil, typically used in the construction of embankments and dykes, with the aim of providing a better understanding of the consequences of drying-wetting cycles on the response of the material over time. Experimental tests were performed to study the impact of drying-wetting cycles on the water retention, hydraulic conductivity and fabric of compacted specimens. Fabric changes are documented to take place even without significant volumetric strains, promoting an irreversible increase in the hydraulic conductivity and a reduction in the capacity to retain water compared to the as-compacted soil. The fabric changes are interpreted and quantified by means of a hydromechanical model, which accounts for the evolving pore size distribution at different structural levels. The proposed model reproduces quite well the microstructural observations, together with the evolution of the water retention behaviour and of the hydraulic conductivity.

Key words:

Compacted silt; drying-wetting cycle; water retention; hydraulic conductivity; microstructure; hydromechanical model

Number of words: 7350
Number of figures: 13
Number of tables: 6

3

80 **1.   Introduction**

81 Earth structures are widely exposed to interactions with the environment, especially to variations in the atmospheric

82 conditions and in the ground water level. When the environmental conditions become severe, failure of these structures

83 may occur causing economic losses and casualties. Far from failure, atmospheric changes and water level oscillations

84 constitute repeated hydraulic loads inducing drying-wetting cycles, which significantly affect the geotechnical

85 behaviour of earth structures and slopes because of their impact on the distribution of water pressure (e.g. Vaughan et

86 al. 2004; Smethurst et al. 2006; Rouainia et al. 2009).

87 Soil-atmosphere interactions are mainly due to precipitations and to seasonal variations of air relative humidity and

88 temperature. These processes may lead to substantial changes in soil water content and suction, particularly within

89 superficial soil layers (e.g. Croney 1977; Albright et al. 2004; Smethurst et al. 2006). Calabresi et al. (2013) monitored

90 the suction and the water content within a soil embankment at Viadana, along the Po River in the North of Italy. In

91 proximity of the phreatic surface, a zone deeply influenced by the level of impounded water and by capillarity

92 phenomena, very small variations in suction and moisture content occurred. Instead, suction and water content

93 oscillated between extreme values in superficial layers, mainly due to Relative Humidity (*RH*) changes in air (between

94 30 % and 100 %) during the inspection time period (April to October 2001). Such *RH* oscillations represent hydraulic

95 loads that can significantly influence the efficiency of dykes, embankments and also of covers of waste contaminant

96 landfills consisting of soils compacted with high compaction efforts (e.g. Daniel 1987). Benson et al. (2007)

97 characterized the hydraulic behaviour of soils used for water balance covers at the time of construction and a few years

98 after placement. Over time, generally the hydraulic conductivity increased and the air entry value decreased. Similar

99 effects on the hydraulic behaviour of unsaturated soils have been related to desiccation cracks (Drumm et al. 1997;

100 Albrecht and Benson 2001), to freeze-thaw cycles (Benson et al. 1995; Chapuis 2002), and to plant root growth

101 (Smethurst et al. 2006). For all cases, the detected changes in the hydraulic behaviour suggest void ratio and/or fabric

102 evolution.

103 The assessment of the long-term behaviour of low activity compacted soils is fundamental to properly understand and

104 predict the performance of geotechnical structures, such as dykes and embankments, which are mostly built with these

105 materials. However, little attention has been paid to the effects of hydraulic loading on the fabric and hydraulic

106 behaviour of low activity compacted soils, while many works have studied these effects for compacted soils of

107 moderate to high activity (e.g. Sharma 1998; Alshihabi et al. 2002; Cui et al. 2002; Fleureau et al. 2002; Lloret et al.

108 2003; Alonso et al. 2005; Cuisinier and Masrouri 2005; Nowamooz and Masrouri 2009; Airò Farulla et al. 2010;

109 Romero et al. 2011).

4

110   This paper aims to investigate the evolution of the hydraulic behaviour and of the microstructure of a low activity silty

111   soil exposed to drying-wetting cycles such as those expected to act on superficial soil layers in temperate climates.

112

113   **2.   Soil properties**

114   The tested soil, collected at Viadana (North Italy), is a clayey silt (grain size distribution in Fig. 1) and it was used in the

115   construction of an experimental embankment for the assessment of earth structures aimed at the containment of floods

116   along the Po river. The same material has been previously studied by different authors (e.g. Nocilla et al. 2006; Vassallo

117   et al. 2007; Calabresi et al. 2013; Azizi et al. 2017).

118   The soil retrieved from different places on site can contain different percentages of clay and sand. The Atterberg limits,

119   grain specific gravity, calcite content, and grain size distribution of the Viadana silt samples used in this investigation

120   are listed in Table 1. The material can be classified as low plasticity silt (ML) according to ASTM D2487, with a

121   plasticity index equal to $PI = 8.3\%$. The activity index is $A = 0.4$, a value typical of low activity soils.

122   According to X-ray diffraction, the main mineralogical constituents are quartz, calcite and clay minerals of low to

123   moderate activity (mainly kaolinite, chlorite and illite).

124

125   **3.   Specimen preparation and drying-wetting cycles**

126   The collected material was dried and mechanically ground. The specimens were prepared by statically compacting the

127   soil at a dry density $\rho_d = 1680$ kg/m^3 and at a gravimetric water content $w = 20$ %. For each specimen, the dry soil

128   powder was initially sprayed and hand-mixed with demineralised water according to the target water content, sealed in

129   plastic bags and kept hanging over distilled water in a sealed humid container for 48 hours allowing water content

130   equilibration. The wet soil was then placed in a rigid ring having a diameter of 50 mm. An axial force was gradually

131   applied until the desired height (20 mm) was achieved. To avoid the generation of excess pore pressure that might affect

132   homogeneity, a low rate of axial displacements (0.15 mm/min) was imposed during loading. After compression, the

133   specimen was sealed with an impermeable plastic film and kept hanging over distilled water in a closed container for

134   the following 24 hours to allow for water content equilibration. No significant water content changes occurred during

135   this stage. The water content and the dry density of the specimens are similar to those adopted in situ for the

136   experimental embankment (Rojas et al. 2010).

137   Six specimens were used to characterise the microstructure and to study the hydraulic behaviour after compaction. Their

138   dry density (ρ_d), water content (w), void ratio (e), degree of saturation (S_r) and suction (s) are reported in Table 2. Other

139   eight specimens were used to study the effects of repeated hydraulic loads on the water retention, hydraulic conductivity

140 and microstructure. These specimens were subjected to 3 and 6 drying-wetting cycles, namely, "3D/W" and "6D/W".

141 Drying was imposed by placing the specimens within the holder ring above a rigid mesh. Evaporation of water occurred

142 across the mesh and towards the laboratory environment, at controlled temperature and relative humidity. The

143 temperature was $T = 21°C$ (± 0.5 °C). The relative humidity was double-checked and measured to be around $RH =$

144 38.5% (the combination of relative humidity and temperature corresponds to a total suction $\psi = 129$ MPa according to

145 the psychrometric law). The weight and the height of the specimens were measured to track changes in water content

146 and volume. For each of the drying steps, the water content decreased until equilibrium was established after about 120

147 hours, reaching the same value of $w = 0.38$ % at the end of all cycles. During drying, an axial stress of 10 kPa was

148 applied. No significant radial strains were induced and shrinkage of the specimen occurred uniaxially.

149 Wetting took place in the same mould used for static compaction, through a plastic porous disc at the bottom, which

150 was connected to a water pressure line to introduce water into the specimen. A small pressure head of 5 kPa was

151 imposed to maintain the pressure gradient adequately low, thus minimising possible effects of transient high water

152 pressures on the soil volume and microstructure. Water filled the pores gradually while the air was escaping through a

153 tiny passage conduit at the top of the mould. The mass of water injected was measured with a water volume indicator

154 and the average injection rate was about 500 mm^3/h. Wetting was stopped when the water content of the specimens was

155 equal to the one at compaction ($w = 20$%). Vertical displacements were allowed during wetting while radial ones were

156 constrained by the holder ring. After the drying-wetting cycles, the specimens were wrapped up in plastic bags and kept

157 hanging over distilled water in a closed container for at least 5 days to ensure water content homogenization. The size of

158 each specimen was then measured. Fig. 2 shows the evolution of water content with time along one drying-wetting

159 cycle.

160 The filter paper technique was used to measure suction after compaction and after the drying-wetting cycles. The

161 calibration curve of Leong et al. (2002) was adopted. The measurements were very consistent with the water retention

162 data of these specimens (see section 5.1 for comparison). The average measured suction of as-compacted specimens

163 was $s = 33$ kPa, whereas the one of 6D/W specimens was $s = 5$ kPa.

164

165 **3.1   Mechanical response during drying-wetting cycles**

166 Fig. 3 shows the volume strains ε_v and water content w of the 3D/W and 6D/W specimens as a function of the number

167 of cycles. First drying caused a relatively small shrinkage. The contractive volumetric strains at the end of drying

168 increased during the first two or three cycles, implying some irreversible volumetric strains, and they were almost

169 constant at the end of the following cycles during which the specimens showed nearly reversible behaviour. Negative

6

170   strains (expansion) were evident at the end of the first wetting stage, despite the water content being the same as

171   preparation. The expansion strains also stabilized after three cycles.

172

173   **4.   Experimental methods**

174   The hydraulic behaviour and the fabric evolution were studied by different tests, using the techniques summarised in

175   Table 3. Water Retention Curves (WRC) were determined imposing matric suction s with the axis translation technique

176   ($s \leq 400$ kPa) and imposing total suction ψ with the vapour equilibrium technique ($\psi \geq 3$ MPa). The axis translation

177   technique was adopted in a suction controlled oedometer, where an axial net stress $\sigma_{net} = 50$ kPa was applied. A

178   sequence of matric suction $s = 10, 50, 200, 300, 350$ and 400 kPa was imposed over drying. The specimens were then

179   removed from the oedometer and placed in a desiccator with saturated salt solutions, whose total suctions at the

180   laboratory temperature were measured with a WP4 Dewpoint Potentiometer. The following total suctions were

181   imposed: $\psi = 3.6, 8.8, 21.8, 40.1$ and 82 MPa (using the saturated K_2SO_4, KNO_3, KCl, $NaNO_3$ and $Ca(NO_3)_2$ 4 H_2O

182   solutions, respectively). An axial net stress of 20 kPa was imposed during this phase. For each imposed ψ, the

183   specimens were kept in the desiccator until equilibrium was established. Their weight and volume were sequentially

184   measured. After equilibrium at $\psi = 82$ MPa, wetting was induced by imposing the same suctions of the drying path in

185   reversed order. The water retention data are hereby presented in terms of matric suction. The matric suction s was

186   obtained as the difference between the total suction ψ and the osmotic suction π for each stage where the vapour

187   equilibrium technique was applied. The osmotic suction was evaluated as follows: one specimen at the initial water

188   content and void ratio was squeezed (Iyer 1990) to expel a mass of pore water sufficient for electrical conductivity

189   measurements. The electrical conductivity of the pore water was $E.C. = 3.70$ mS/cm, which is consistent with a

190   molarity $M = 0.039$ mol/l of a NaCl solution. For each stage of the Vapour Equilibrium path, the actual molarity was

191   evaluated assuming that only water evaporates, so that the ratio of the dissolved salt mass to the solid fraction of the soil

192   remains constant. This molarity was converted into electrical conductivity - accounting for the decrease of the mobility

193   of ions in concentrated solutions. For each stage, π was related to the estimated electrical conductivity through the

194   graph reported by Fredlund and Rahardjo (1993) (originally from USDA Agricultural Handbook 1950), which was

195   fitted with the relationship $\pi = 31.9 \times E.C.^{1.07}$ (units kPa and mS/cm). The empirical relationship between the osmotic

196   suction and the water content for the tested specimens was then found to be $\pi = 70.29 \times w^{-1.06}$ (w is non-dimensional).

197   The hydraulic conductivity of the saturated specimens was obtained by means of constant head permeability tests. The

198   specimens were saturated by injecting water while the hydraulic head was kept constant until a steady flow of water

199   took place. The hydraulic conductivity in unsaturated conditions was determined by back analysis of the water content

200   changes measured during the water retention tests.

201   Insights on the fabric of specimens at different states were provided by Pore Size Distribution (PSD) curves and by

202   direct observations with Environmental Scanning Electron Microscope (ESEM) pictures. The PSD curves were

203   determined through Mercury Intrusion Porosimetry (MIP) carried out using a Micromeritics AutoPore IV 9500, in

204   which two different systems were operated: a low mercury pressure system (between 0 and 0.345 MPa) and a high

205   mercury pressure system (between 0.345 MPa and 228 MPa). These operating systems allow mercury to intrude pores

206   with radii ranging between 0.0035 μm and 200 μm. Cylindrical specimens with height and diameter of 10 mm were

207   trimmed from the original ones for MIP analyses. The fabric of the wet specimens was preserved by dehydration using

208   the freeze-drying technique (Delage and Pellerin 1984). All specimens were then weighted and placed in the

209   penetrometer, followed by evacuation of gas from the chamber to generate the vacuum condition.

210

211   **5.   Effects of repeated hydraulic loads on the hydraulic behaviour**
212   **5.1   Water retention behaviour**

213   Fig. 4(a) shows the water retention curves of the as-compacted specimens and of the specimens subjected to drying-

214   wetting cycles in terms of $\log(s)$-S_r. A reduced capacity for retaining water of the D/W specimens was evident along

215   both the main drying and the main wetting paths, where the water content of the D/W specimens was always noticeably

216   smaller than that of the as-compacted specimen for suction $s < 20$ MPa. Drying–wetting effects were not observed at

217   very high suction ($s \geq 20$ MPa). Consistently with the reversible mechanical response after the third drying-wetting

218   cycle, the drying WRC of the 6D/W specimen was quite similar to the one of the 3D/W specimen. Volume changes

219   taking place during the water retention tests were very small.

220   The initial void ratio of the D/W specimens was slightly smaller than the one of the as-compacted specimens because

221   the formers had a slightly higher volume decrease under the axial net stress $\sigma_{net} = 50$ kPa imposed in the suction

222   controlled oedometer. Volume changes taking place during the water retention tests were very small (Fig. 4(b)).

223   Altogether, the results showed that the water retention behaviour of the D/W specimens differs from the original one

224   mainly because of changes in the soil fabric, mostly occurring during the first cycles, rather than because of changes in

225   the void ratio.

226   Different water retention domains can be identified: a high suction range with almost no hysteresis ($s \geq 20$ MPa), an

227   intermediate suction range and a low suction range, which can be distinguished from each other by substantial changes

228   in the shape of the curves as shown in Fig. 4(c) in terms of water ratio ($e_w = S_r.e$) and suction. The size of the two latter

8

229   domains, which are separated by the inflection point of the WRC, evolved during the drying-wetting cycles (see also

230   Romero and Vaunat 2000; Aubertin et al. 2003; Romero et al. 2011; Della Vecchia et al. 2015).

231

232   **5.2   Hydraulic conductivity**

233   The average saturated hydraulic conductivity of the specimens, evaluated by constant head tests, was $K_s = 1.1 \times 10^{-9}$ m/s

234   for the as-compacted specimens and $K_s = 1.3 \times 10^{-8}$ m/s for the 6D/W specimens. The hydraulic conductivity in

235   unsaturated conditions was determined by back analysis of the water content changes measured during the water

236   retention tests. The Finite Element code COMSOL was used to reproduce the water outflow along the suction

237   equalization phases of the drying paths (in the range $10 \leq s \leq 400$ kPa) and the hydraulic conductivity was then obtained

238   relying on Richard's equation (e.g. Eching et al. 1993; van Dam et al. 1994; Fujimaki and Inoue 2003):

$$\frac{\partial \theta}{\partial t} = -\frac{\partial}{\partial z} \frac{K_w(S_e)}{\gamma_w} \frac{\partial s}{\partial z} - 1]} \tag{1}$$

239

240   where γ_w is the specific weight of water, $\theta = \frac{e_w}{1+e}$ is the volumetric water content, z is the spatial coordinate, t is the

241   time and K_w is the hydraulic conductivity in unsaturated conditions. The effective degree of saturation S_e is defined as

242    $S_e = \frac{S_r - S_{res}}{1 - S_{res}}$, where $S_{res} = 0.07$ is the residual degree of saturation. For each suction increment, the decrease in water

243   content was expressed in terms of moisture capacity $C(s) = \frac{\partial \theta}{\partial s}$ determined from the WRC and the current hydraulic

244   conductivity was approximated with its average constant value. The following equation was then solved:

$$C(s)\frac{\partial s}{\partial t} = -\frac{K_w(S_e)}{\gamma_w}\frac{\partial^2 s}{\partial z^2} \tag{2}$$

245

246   An optimization procedure was implemented to determine the best values of K_w for the as-compacted and 6D/W

247   specimens. In the experiments, the water flow rate depended also on the impedance of the bottom porous stone, through

248   which the flow took place. Therefore, the porous stone, having height 7 mm and saturated hydraulic conductivity

249   1.21×10^{-9} m/s, was also modeled. In the numerical simulation, suction values were imposed at the bottom of the porous

250   stone, while a no flow condition was imposed at the top boundary.

251   Fig. 5(a) compares the changes in the volumetric water content $\Delta \theta$ measured during the test with the numerical

252   predictions. According to the back analysis, the hydraulic conductivity of the 6D/W specimen is greater than the one of

253   the as-compacted specimen over the whole saturation range (Fig. 5(b)). This general increase of hydraulic conductivity,

254   observed also at full saturation, is related to the fabric changes taking place at almost constant volume, which are

255   discussed in detail in the following.

9

256

6. Effects of repeated hydraulic loads on microstructure
6.1 Fabric arrangement

259 ESEM pictures of the as-compacted and 6D/W specimens shown in Figs. 6(a), 6(b) and 6(c) portray the soil fabric and

260 the pore network. These pictures were taken while setting the temperature $T = 10\ °C$ and the vapour pressure $u_v = 630$

261 Pa in the chamber, with a corresponding relative humidity $R.H. = 53\%$. The silt and clay fractions are well evident. The

262 clay fraction consists of single clay particles (denoted by 'C') and of aggregations of clay particles (clay peds). Silt

263 particles (denoted by 'S') are also evident.

264 The radii of the pores between peds and between large particles and peds, recognised at the lower magnification of Figs.

265 6(a), 6(b) and 6(d), are of the order of a few microns. The radii of the pores within the peds appear to be clearly below 1

266 μm including those recognised at the higher magnification of Fig. 6(c) and those invisible at this magnification. This

267 may suggest three classes of pores including micropores and mesopores inside the peds and macopores external to the

268 peds, as it will be discussed in the next section.

269 Fig. 6(d) shows an ESEM image of the 6D/W dry specimen. This figure shows that single peds might break into smaller

270 peds, separated by fractures having the size of macropores, which suggests that drying-wetting cycles induce breakage

271 of peds, increasing the macroporosity. Nonetheless, neither cracks nor fissures at the surface of the specimens were

272 evident to the naked eye.

273

6.2 Pore size distribution

275 The pore size distributions presented in Fig. 7(a) describe the following four conditions: As-compacted ($w = 20\%$), after

276 first drying ('As-compacted dry', $w = 0.38\%$), at the end of the sixth drying stage ('6D/W dry') and at the end of the

277 sixth wetting stage ('6D/W'). The PSD curves are clearly bi-modal, with a dominant peak in correspondence of a pore

278 radius smaller than 1 μm and another peak in the range of 5-10 μm. Microstructural changes from the as-compacted

279 condition to the 6D/W condition are evident. The as-compacted and the as-compacted dry specimens have a dominant

280 pore radius $r = 609$ nm, but the size of the peak is greater for the dry specimen. The PSDs of the 6D/W dry and 6D/W

281 specimens overlap very well, both showing an increase of the dominant pore radius to $r = 917$ nm. The radius of the

282 smaller PSD peak shifts from about 5 μm (as-compacted) to about 8 μm (wet state of the 6D/W), while it remains about

283 5 μm for the 6D/W dry. The evolution of the PSDs shows that the soil fabric is sensitive to repeated hydraulic loads,

284 confirming that fabric changes take place even without significant changes in the total volume.

285 The total intruded void ratio e_{int} was smaller than the total void ratio e (Fig. 7(b)) since not all the available porosity was

286 intruded by mercury. This difference is due both to very large pores, filled by mercury at very low pressures, whose

287   volume is not measured during intrusion, and to very small pores which are not intruded even at very high pressures.

288   The fraction of void ratio associated to the very small pores is assumed to be equal to the water ratio corresponding to

289   irreducible saturation, and it is about 0.04 for all specimens. The non-intruded fraction of void ratio associated with very

290   large pores is then estimated as the difference between the non-intruded void ratio and 0.04.

291   Based on the PSDs, three classes of pores (micropores, mesopores and macropores) are identified. This allows

292   individuating a microstructural void ratio e_{Mi}, a mesostructural void ratio e_{Me} and a macrostructural void ratio e_{Ma}:

$$e_{Mi} = \frac{V_{vMi}}{V_s}, e_{Me} = \frac{V_{vMe}}{V_s}, e_{Ma} = \frac{V_{vMa}}{V_s} \tag{3}$$

293

294   where V_{vMi} is the volume of the micropores, V_{vMe} is the volume of the mesopores, V_{vMa} is the volume of the macropores

295   and V_s is the volume of the solid phase. The total void ratio e is then:

$$e = e_{Mi} + e_{Me} + e_{Ma} \tag{4}$$

296

297   Selecting a criterion to discriminate between different classes of pores always involves some degree of arbitrariness,

298   and the choices that were made in the elaboration of the data are presented here. Micropores are defined as those pores

299   still saturated at very high suctions, and whose behaviour during drying-wetting cycles is completely reversible. On the

300   basis of the results in Fig. 4(c), the corresponding void ratio is $e_{Mi} = 0.06$ for all conditions. The threshold pore radius

301   separating micropores from mesopores R_{Mi} is determined as the radius at which the following condition is satisfied:

$$e_{Mi} = \int_{3.5}^{R_{Mi}} \frac{PSD(r)}{r.\ln(10)}.dr + 0.04 \tag{5}$$

302

303   where 3.5 nm is the smallest pore radius intruded by MIP and *0.04* is the void ratio corresponding to the very small non

304   intruded pores. By imposing $e_{Mi} = 0.06$ it follows $R_{Mi} = 11$ nm. Note that the argument function of the integral in eq. (5)

305   follows logically from the definition of the PSD as the incremental fraction of intruded void ratio with respect to the

306   logarithm of the pore radius, as discussed for instance by Della Vecchia et al. (2015).

307   Mesopores are identified with the larger pores within the clay peds. According to the ESEM pictures (Fig. 6), their radii

308   are expected to be smaller than 1 μm. MIP analyses of specimens loaded to increasingly higher net stresses showed a

309   progressive reduction of the volume of the pores having radii greater than the dominant peak, and no clear effects on

310   pores whose radius was smaller (Azizi et al. 2018). The evidence confirms the shared view that mechanical

311   compression mostly affects pores external to clay aggregates (or macro-pores, see e.g. Delage and Lefebvre 1984;

312   Tarantino and De Col 2008; Koliji et al. 2010). Therefore, the threshold pore radius R_{Me} separating the macropores from

313   the mesopores was selected as the pore radius of the dominant peak of the PSD (equal to 609 nm for the as-compacted

314   and first drying states, and equal to 917 nm for the 6D/W dry and 6D/W wet states). V_{vMe} is the volume of pores whose

11

315   entrance radius is between R_{Mi} and R_{Me}; the values of e_{Me} were obtained through Eq. (3). Finally, values of e_{Ma} for each

316   state were determined by applying Eq. (4).

317   The threshold pore radii separating the different classes of pores and the void ratios e_{Mi}, e_{Me} and e_{Ma} are summarised in

318   Table 4.

319

320   **6.3   Fabric evolution based on conjugate analysis of MIP and ESEM data**

321   Repeated hydraulic loads induce two different effects at the mesostructural level. Firstly, the mesostructural void ratio

322   of the 6D/W states (e_{Me} = 0.32) is smaller than the one of the as-compacted state (e_{Me} = 0.36). This suggests that the peds

323   experience irreversible strains, and their contraction during drying is not fully recovered during wetting. Since the final

324   suction is smaller than the one at preparation, the behaviour of the peds cannot be elastic, otherwise drying-wetting

325   cycles would lead to a net expansion of the peds. Secondly, the radius of the larger mesopore increases from 609 nm to

326   917 nm (Table 4).

327   While the overall void ratio remains constant upon the repeated hydraulic loads, the macrostructural void ratio evolves

328   from the initial e_{Ma} = 0.24 of at the as-compacted state to e_{Ma} = 0.28 of the 6D/W wet state. Simultaneously, the

329   dominant radius of macropores increases from 5030 nm to 8230 nm. Contraction of the peds is responsible for larger

330   macroporosity and larger individual macropores, thanks to stiffening effect of the granular silt skeleton, which is less

331   sensitive to water content changes (as observed also for Barcelona clayey silt by Romero et al. 2014). The lower air

332   entry value of the peds, the larger macrostructural void ratio and the larger pore radii of the macrostructure of 6D/W

333   samples all concur to explain the significant change of the water retention capacity and the increase in hydraulic

334   conductivity.

335   The experimental WRCs and those predicted on the basis of MIP results are compared in Fig. 8. Since mercury is a non-

336   wetting fluid, MIP data can be used to derive a water retention curve by assuming that its penetration is equivalent to air

337   intrusion during a drying path. The radius r of a pore determines both the matric suction s during drying and the

338   pressure of penetrating mercury p (e.g. Romero et al. 1999), so that:

339

$$s = \frac{4\sigma cos\theta_w}{r} ; p = -\frac{4\sigma_{Hg}cos\theta_{Hg}}{r} ; s = -\frac{\sigma cos\theta_w}{\sigma_{Hg}cos\theta_{Hg}}p \approx 0.196\,p \qquad (6)$$

340   where σ = 0.072 N/m is the surface tension of water and θ_w = 0° is the contact angle for the air-water interface, σ_{Hg} =

341   0.484 N/m is the surface tension of mercury and θ_{nw} = 140° is the contact angle between mercury and the particle

342   surface.

12

343   The WRC is derived from MIP data at the fixed void ratio of the tested sample. On the contrary, single values of water

344   retention determined experimentally over drying/wetting paths reflect the concomitant shrinkage and swelling occurring

345   during the test. Direct comparison of the two is hardly significant in the case of active clays (Romero et al. 2011), for

346   which numerous PSDs are required to determine the complete retention domain (Della Vecchia et al. 2015). However,

347   in the case of Viadana silt changes in total void ratio are negligible, and the MIP derived WRCs reproduce quite well

348   the experimental water retention both along first drying and along drying after 6D/W cycles. The difference between the

349   first drying and the following drying paths shows the relevance of internal microstructural rearrangement for the tested

350   silty soil, though its composition include no relevant percentage of active clay minerals particularly sensitive to

351   physico-chemical phenomena.

352

353   **7.   Modelling macroscopic behaviour accounting for microstructural evolution**
354   **7.1   Coupled hydromechanical model**

355   The experimental results show that both the hydraulic behaviour and the fabric of Viadana silt evolve with drying-

356   wetting cycles. The volume of the peds and the water retention properties undergo irrecoverable changes during the first

357   cycle, and stabilise afterwards. To assist in the interpretation of the data and to quantify the effects of the drying-wetting

358   cycles, a microstructural framework is needed. Table 4 suggests that the microstructural void ratio e_m remained

359   constant, so it is not strictly necessary to consider the micro-pores separately from the meso-pores when formulating a

360   microstructural model, since both classes of pores are found within the peds. A double porosity framework was then

361   used which allows to distinguish between the micro-meso and the macro fabric levels and to incorporate microstructural

362   changes.

363   A model for the volumetric response is introduced to this extent. Two structural levels are defined and described based

364   on their respective void ratios, one pertaining to the void space within the peds (intra-peds) and the other external to the

365   peds (macrostructure). The overall behaviour of the material follows as the superposition of the two structural levels

366   where the two fabric levels are assumed to be in hydraulic and mechanical equilibrium. Two sets of hydromechanical

367   variables are defined: matric suction and Bishop type effective stress as stress variables, and water ratio (or degree of

368   saturation) and volume strain (or void ratio) as strain variables. The proposed model shares fundamental hypotheses

369   with double porosity models formulated for expansive soils (e.g. Gens and Alonso 1992; Alonso et al. 1999; Mašin

370   2013, Musso et al. 2013) whereas it adopts the elastoplastic framework for the behaviour of the peds based on the

371   microstructural observations. The asymptotic behaviour resulting from an increasing number of drying-wetting cycles is

372   then reproduced as a direct consequence of the proposed hardening laws, which are discussed in the following.

373

13

374   **7.1.1   Fabric levels and strain variables**

375   Micropores and mesopores belong to the intra-peds porosity, while macro-pores are associated with the porosity

376   external to the peds. The intra-peds void ratio e_m and the macrostructural void ratio e_{Ma} are defined as:

$$e_m = e_{Me} + e_{Mi} = \frac{V_{vMe} + V_{vMi}}{V_s} = \frac{V_{vm}}{V_s}, e_{Ma} = \frac{V_{vMa}}{V_s} \tag{7}$$

377   where V_{vm} is the volume of the intra-peds voids.

378   The intra-peds water ratio e_{wm} and the macrostructural water ratio e_{wMa} are obtained imposing that the total mass of

379   water stored within the soil is the sum of the mass of water within the peds and the mass of water in the macroporosity:

$$e_w = e_{wMa} + e_{wm} = e_{Ma}S_{rMa} + e_m S_{rm} \tag{8}$$

380

381   with $e_{wm} = \frac{V_{wm}}{V_s}$, $e_{wMa} = \frac{V_{wMa}}{V_s}$, $S_{rm} = \frac{V_{wm}}{V_{vm}}$, $S_{rMa} = \frac{V_{wMa}}{V_{vMa}}$, where V_{wm} is the volume of water within the peds, V_{wMa} is the

382   volume of water within the macropores, S_{rm} is the intra-peds degree of saturation, S_{rMa} is the macrostructural degree of

383   saturation.

384

385   **7.1.2   Stress variables**

386   Two stress variables are employed including a mechanical constitutive stress and suction. The first one is assumed to

387   depend on the net stress (σ_{net}), the effective degree of saturation (S_e) and the suction in the form:

$$\boldsymbol{\sigma}' = \boldsymbol{\sigma}_{net} + S_e s \boldsymbol{I} \tag{9}$$

388   where Eq. (9) is a general expression, which can be used to describe the average mechanical stress acting on the soil

389   skeleton or on each structural level (macrostructural stress σ'_{Ma} or peds stress σ'_m), by using the corresponding effective

390   degree of saturation. As in most of the previous double porosity models, the total (net) stress acting on each level is

391   assumed to be the same (e.g. Alonso et al. 1999; Mašin 2013; Wang et al. 2015). The second stress variable is the

392   matric suction. Similar stress variables have been adopted by different authors (e.g. Jommi 2000; Romero and Jommi

393   2008; Della Vecchia et al. 2013).

394

395   **7.1.3   Water retention model**

396   According to Eq. (8), the overall WRC in terms of water ratio $e_w(s)$ is expressed as the superposition of the WRCs of

397   the two fabric levels (e.g. Durner 1994; Casini et al. 2012; Della Vecchia et al. 2015):

$$e_w(s) = e_{Ma}\left[\frac{1}{1 + (\alpha_{Ma}s)^{n_{Ma}}}\right]^{m_{Ma}} + e_m\left[\frac{1}{1 + (\alpha_m s)^{n_m}}\right]^{m_m} \tag{10}$$

14

398 where n_{Ma}, m_{Ma}, α_{Ma} and n_m, m_m, α_m are the parameters of the van Genuchten's model (1980) for macro-pores and

399 intra-peds pores, respectively. The total degree of saturation is obtained by the sum of S_{rMa} and S_{rm} weighted by the

400 corresponding volumetric fractions.

401 A relationship between water ratio and suction in the scanning domain is needed for the simulation of the transition

402 from drying to wetting branches (and vice versa) over the hydraulic cycles. The incremental form of equation (10)

403 reads:

$$de_w(s) = de_{wMa} + de_{wm} = [S_{rMa}de_{Ma} + e_{Ma}dS_{rMa}] + [S_{rm}de_m + e_mdS_{rm}] \tag{11}$$

404

405 The scanning curves are predicted by replacing $dS_r = -k_{sc}ds$ for each structural level:

$$de_w^{sc}(s) = \left[\frac{e_{wMa}}{e_{Ma}}de_{Ma} - e_{Ma}k_{sc}ds\right] + \left[\frac{e_{wm}}{e_m}de_m - e_mk_{sc}ds\right] \tag{12}$$

406 where k_{sc} controls the slope of the scanning curves. The behaviour in the scanning domain is assumed to be reversible.

407

408 **7.1.4   Mechanical model**

409 Water retention depends on the macrostructural and intra-peds void ratios, whose evolution is predicted by a mechanical

410 model. Wheeler et al. (2003) proposed an elastoplastic framework that couples hydraulic hysteresis with stress-strain

411 behaviour. A similar framework is adopted to reproduce the mechanical behaviour of the peds coupled with the intra-

412 peds water retention. The peds constitutive stress (σ'_m) is employed to predict the volumetric changes of the peds,

413 influenced by the intra-peds effective degree of saturation. On the other hand, intra-peds void ratio changes affect the

414 intra-peds water ratio, because both the water storage capacity and the air-entry value evolve.

415 Hardening is introduced including two yielding criteria: one associated with mechanical straining of the peds and the

416 other responsible for irreversible changes of the peds water ratio. As shown in Fig. 9(a), the former yielding occurs

417 when the stress path reaches the loading collapse (LC) curve whereas the latter is triggered if the stress path reaches the

418 suction increase (SI) curve during drying, or the suction decrease (SD) curve during wetting. These yield curves are

419 expressed as:

$$\text{LC: } \sigma'_m = \sigma'^*_m, \text{ SI: } s = s_I, \text{ SD: } s = s_D \tag{13}$$

420

421 Where σ'^*_m is the peds yield stress, s_I is the suction increase yield curve and s_D is the suction decrease yield curve.

422 Increments of volumetric strains of the peds occurring inside the elastic domain ($\Delta\varepsilon_m^e$) are given by:

$$d\varepsilon_m^e = \frac{\kappa_m d\sigma'_m}{(1 + e_m)\sigma'_m} \tag{14}$$

423

15

424   where κ_m is the elastic compliance for the intra-peds void ratio. For stress paths within the elastic domain, the degree of

425   saturation evolves along the scanning curves.

426   If yielding occurs directly on the SI, it induces water ratio changes on the main drying WRC accompanied with

427   hardening of the LC, whereas direct yielding on the SD induces water ratio changes on the main wetting WRC

428   accompanied with softening of the LC. If yielding occurs on the LC, it produces plastic volumetric strains with a

429   coupled outward movement of the SI and inward movement of the SD. The SI and the SD evolve together:

$$\frac{ds_I}{s_I} = \frac{ds_D}{s_D} \tag{15}$$

430   When yielding occurs due to SI or SD, the hardening law is:

$$d\sigma'^*_m = h_{lC}\sigma'^*_m \frac{ds_I}{s_I} \tag{16}$$

431   h_{lC} controls the coupled movement of the LC due to SI or SD yielding. The increments of plastic volumetric strains (d

432   ε^p_m) due to yielding of LC curve are

$$d\varepsilon^p_m = \frac{(\lambda_m - \kappa_m)d\sigma'^*_m}{(1 + e_m)\sigma'_m} \tag{17}$$

433   where λ_m and κ_m are model parameters and the hardening law in this case is given by,

$$ds_I = h_s s_I \frac{d\sigma'^*_m}{\sigma'^*_m} \tag{18}$$

434   where h_S controls the coupled movement of SI and SD.

435   The general expression for plastic strain increment can be derived through Eqs. (16) and (17):

$$d\varepsilon^p_m = \frac{(\lambda_m - \kappa_m)}{(1 + e_m)(1 - h_s h_{lC})}\left(\frac{d\sigma'^*_m}{\sigma'^*_m} - h_{lC}\frac{ds_I}{s_I}\right) \tag{19}$$

436

437   Two flow rules are given, respectively associated to the yielding on the SI and SD curves:

$$\frac{d\varepsilon^p_m}{de_{wm}} = 0 \tag{20}$$

438   and associated to the yielding on the LC curve:

$$\frac{de_{wm}}{d\varepsilon^p_m} = 0 \tag{21}$$

439

440   Changes of the intra-peds void ratio are written in the form:

$$de_m = -d\varepsilon_m(1 + e_m) = -(d\varepsilon^e_m + d\varepsilon^p_m)(1 + e_m) \tag{22}$$

441

442   The influence of the mechanical effects on the WRC of the peds is shown in Fig. 9(b). The specimens were subjected to

443   a wide range of suction and the peds were almost completely dry at the end of drying, whereas they were entirely

444   saturated at the end of wetting. SI yielding occurred when air entered the saturated peds (suction greater than their air-

445   entry value), and SD yielding occurred along wetting when the degree of saturation of the peds S_{rm} was greater than the

446   residual one.

447   A similar framework may also be adopted also for the macrostructural fabric level. However, changes of the

448   macrostructural void ratio were evaluated here as the difference between the changes of the total void ratio and that of

449   the intra-peds void ratio. A simple elastic expression was used for the increments of overall volume strains ($d\varepsilon_v$):

$$d\varepsilon_v = \frac{\kappa \cdot d\sigma'}{(1 + e)\sigma'} \tag{23}$$

450   where κ is the elastic logarithm compressibility. Hence, the total void ratio changes are:

$$de = -d\varepsilon_v(1 + e) \tag{24}$$

451   and the macrostructural void ratio changes are:

$$de_{Ma} = de - de_m \tag{25}$$

452   Eqs. (22) and (25) give the evolution of the void ratio of macro- and intra-peds pores which contribute to the coupled

453   water retention model (Eq. (10)).

454

455   **7.2   Calibration of the parameters**

456   The parameters calibration was mostly based on independent tests with respect to the WRCs reproduced. An oedometer

457   test was used to determine the elastic compliances of the overall soil κ and the one of the peds κ_m, which were assumed

458   to have the same value of 0.003, and the preconsolidation stress imposed during compaction, $\sigma'^*_m = 657$ kPa, which

459   identifies the initial position of the LC (see details in Azizi 2016). The initial air entry value of the peds $1/\alpha_m = 236$ kPa

460   was determined by means of the MIP measurements, introducing the radius of the larger mesopore ($r = 609$ nm) into the

461   first one of Eq. 6. According to the model, the air entry value also provides the initial position of the SI, while the SD is

462   set equal to the suction imposed at the beginning of the water retention test (SD = 10 kPa). The parameters for the WRC

463   of the macro-structure were determined imposing the best fit between the experimental water ratio of the macrostructure

464   ($e_{wMa} = e_w - e_m$) along the first drying branch for suction values smaller than the air entry value of the peds (Table 5).

465   The elasto-plastic compliance λ_m was calibrated to capture the amount of contraction of the peds during the first drying

466   stage, as determined with MIP. The scanning parameter k_{sc} was calibrated upon water retention tests presented by Azizi

467   et al. (2017). The parameters h_{lC} and h_s were calibrated to obtain a reversible behaviour after three cycles.

17

468   The van Genuchten's parameters of both structural levels evolve along the hydraulic cycles to adequately reproduce the

469   evolution of the water retention. Simple relationships were chosen relating $1/\alpha_{Ma}$ and $1/\alpha_m$ to the saturated water

470   ratios of the macropores e_{wMa}^{sat} and of the peds e_{wm}^{sat}:

$$1/\alpha_{Ma} = (e_{Ma0}/e_{wMa}^{sat})^4/\alpha_{Ma0} \text{ and } 1/\alpha_m = (e_{wm}^{sat}/e_{m0})^{8.2}/\alpha_{m0} \tag{26}$$

471

472   where e_{Ma0} and e_{m0} are the initial macrostructural and intra-peds void ratios of the as-compacted specimen, and $1/\alpha_{Ma0}$

473   and $1/\alpha_{m0}$ are the initial air-entry values of the respective drying curves. The empirical laws described by Eq. (26) were

474   used both for the main drying and the main wetting curves. The parameters of the mechanical model are listed in Table

475   6.

476   The model was employed to predict the final values of α_M and α_m, which determine the WRC after 6 cycles, together

477   with the final values of the hydraulic conductivity and of the relative permeability.

478

479   **7.3   Simulation of drying-wetting cycles: mechanical behaviour and water retention**

480   The void ratio and suction measured during the water retention tests are compared to the model predictions in Fig.

481   10(a). Six drying-wetting cycles were simulated. The evolution of the intra-peds and macrostructural void ratios is

482   presented in Fig. 10(b). Void ratios evaluated on basis of the MIP data are nicely captured. Adopting an elastoplastic

483   framework for modeling the behaviour of the peds allowed properly simulating the decrease of the intra-peds void ratio

484   and the increase of the macro-structural void ratio occurring during the first 3 hydraulic cycles.

485   The modelled changes in intra-peds and macrostructural void ratios rule the evolution of the water retention, whose

486   simulation is introduced in Fig. 11.Fig. 11(a) shows the experimental results and the model predictions for the first

487   drying and wetting cycle in terms of S_r–log(s). The predictions of the degree of saturation of the macropores and of the

488   peds are also provided. Since different air-entry values are defined for the two structural levels, in the suction range 64

489   kPa $< s <$ 236 kPa the peds are still saturated while the macro-pores are desaturating. A similar condition occurs during

490   wetting in the suction range 8 kPa $< s <$ 34 kPa. The changes in the WRCs of the two structural levels due to drying-

491   wetting cycles are given in Fig. 11(b). At the end of each wetting stage, the intra-peds pores are always fully saturated,

492   while, for the same suction, the degree of saturation of the macropores S_{rMa} decreases during the first three cycles. The

493   water retention behaviour of the 6D/W specimens was predicted by simulating 6 drying-wetting cycles imposed to the

494   as-compacted specimen, and it is plotted in Fig. 11(c). The good match between experimental data and predictions

495   shows the capability of the conceptual model to reproduce the evolution of the water retention behaviour over hydraulic

496   cycles.

497   Experimental water retention data of the first drying-wetting cycle and model predictions are re-plotted in Fig. 12(a) in

498   terms of e_w–log(s). The water ratio of peds e_{wm} at the end of the first wetting is smaller than the original one, since the

499   intra-peds void ratio reduces due to plastic strains. On the contrary, the water ratio of macropores e_{wMa} increases. During

500   the first three drying-wetting cycles e_m progressively reduces while e_{Ma} progressively increases, affecting the air entry

501   values of both peds and macropores (Eq. 26). Fig. 12(b) shows the experimental results and model predictions for the

502   6D/W specimen. For both structural domains, the water ratio at the beginning of drying and at the end of wetting is the

503   same since the mechanical behaviour became reversible and the water retention curves cannot evolve further.

504

505

506   **7.4   Model validation exploiting the hydraulic conductivity analysis**

507   The hydraulic conductivity of compacted soils having bimodal pore size distribution is mainly related to the volume and

508   distribution of the larger pores (e.g. Cuisinier et al. 2011; Romero 2013). As a result, the increase in the saturated

509   hydraulic conductivity K_s evidenced in Section 5.2 is justified by the increase of the macrostructural void ratio and can

510   be modeled using a Kozeny-Carman like equation based on e_{Ma} (Romero 2013):

$$K_s = B\frac{e_{Ma}^5}{1 + e_{Ma}} \tag{27}$$

511

512   where $B = 5\times10^{-6}$ m/s was found to adequately simulate the experimental data. The hydraulic conductivity under

513   unsaturated condition K_w is defined as the product of a relative permeability k_r and K_s:

$$K_w = k_r K_s \tag{28}$$

514

515   The relative permeability k_r is controlled by the size of the pores and the shape of PSD. It can be predicted either from

516   the relationships between suction and effective degree of saturation (Mualem 1976):

$$k_r^{(Mualem)} = \frac{K_w}{K_s} = S_e^{1/2}\left[\frac{\int_0^{S_e} dS_e/s}{\int_0^1 dS_e/s}\right]^2 \tag{29}$$

517

518   or as a power law function of the degree of saturation (e.g. Bear 1972), whose exponent is often assumed equal to 3. By

519   admitting that the contribution to flow of the intra-peds pores is negligible, it follows that:

19

$$k_r{}^{(Macro)} = \left(\dfrac{S_r - \dfrac{e_{wm}}{e}}{1 - \dfrac{e_{wm}}{e}}\right)^3 \tag{30}$$

520

521   The values of S_r, e_{wm} and e given by the simulations were introduced in both Eq. (29) and Eq. (30) to obtain the

522   predictions presented in Fig. 13(a), where they are compared to the experimental data based on the back-analysis of

523   Richards' equation. Both expressions captured the experimental data well, although the prediction of the power law

524   expression was found to better match the experimental results.

525   The evolution of K_w during hydraulic cycles is obtained by combining the hydromechanical model with Eq. (27) and

526   Eq. (30). The predictions are compared to the data obtained by the inverse analysis of Richard's equation in Fig. 13(b),

527   where a good match is observed. It is worth noting that since the total void ratio changed reversibly during drying-

528   wetting cycles, the Kozeny-Carman equation, as well as any other model giving an estimate of the hydraulic

529   conductivity based on the total void ratio, would not be able to predict any change in the hydraulic conductivity. On the

530   contrary, the framework developed is able to predict the irreversible increase in macroporosity during drying and

531   wetting cycles, which resulted in the observed relevant increase in the hydraulic conductivity of the investigated soil

532   specimens.

533

534   **8.   Summary and conclusions**

535   While the influence of fabric and fabric evolution on the hydromechanical behaviour of compacted active clays has

536   been studied in detail in the recent years, its relevance on the hydromechanical behaviour of low activity clays and silts

537   has been less explored. These materials are widely used to build earth structures exposed to intensive interaction with

538   water and the atmosphere. Assessment of their response to environmental actions is then relevant for the long-term

539   stability and serviceability of engineering works. This study was aimed to evaluate the impact of typical drying-wetting

540   cycles, occurring at relatively low stresses in earth structures after compaction, on the hydraulic behaviour of a low

541   activity compacted clayey silt used for the construction of water defenses, and to explain the observed behaviour with

542   the aid of microstructural evidences.

543   While the overall volume strains were negligible and became reversible after a limited number of drying-wetting cycles,

544   the hydraulic behaviour was dramatically affected by the hydraulic history in which water retention capacity reduced

545   and hydraulic conductivity increased. The fabric of the tested soil consists of peds of clay particles mixed among silt

546   grains, with larger pores external to the peds and smaller pores within the peds. Microstructural investigation, based on

547   MIP analyses, indicated that the porosity and the volume of the peds decreased mainly during the first cycles.

548   Meanwhile, the fraction of porosity external to the peds increased since the overall volume remained almost constant.

549   Thus, the repeated hydraulic loads induced a sort of hydraulic fabric degradation associated to the development of

550   larger pores.

551   A double porosity model, calibrated on the microstructural observations and accounting for coupling between the

552   hydraulic and mechanical responses, was developed. An important feature of the model was introducing an elasto-

553   plastic behaviour for the clay aggregates, which is usually neglected in similar formulations. Good reproduction of the

554   experimental results was obtained by imposing the dependency of the water retention on the intra-peds and

555   macrostructural void ratios, whose evolution is governed by suction and degree of saturation. Besides, the substantial

556   change in hydraulic conductivity observed at the sample level was explained by means of the fabric changes predicted

557   by the proposed modelling framework. As the soil tested is a low plasticity clayey silt, its behaviour is hardly affected

558   by the sensitivity to water of the constituent minerals, contrarily to active clays. Nonetheless, this investigation shows

559   that the irreversible hydromechanical behaviour of the peds causes substantial changes in the water retention capacity as

560   well as in the hydraulic conductivity of this material. These changes should be considered when the assessment of the

561   hydromechanical behaviour of soils used in earth constructions is required for the design lifetime, since the response of

562   the construction will not be governed only by the soil fabric at the time of compaction.

563

564   **REFERENCES**

565 Airò Farulla, C., Ferrari, A. and Romero, E. 2010. Volume change behaviour of a compacted silty clay during cyclic
566 suction changes. *Canadian Geotechnical Journal*, 47(6): 688-703.

567 Albrecht, B. and Benson, C. 2001. Effect of desiccation on compacted natural clays. *Journal of Geotechnical and*
568 *Geoenvironmental Engineering*, 127(1): 67–76.

569 Albright, W. H., Benson, C. H., Gee, G. W., Roesier, A. C., Abichou, T., Apiwantragoon, P., Lyles, B. F. and Rock, S.
570 A. 2004. Field water balance of landfill final covers. *Journal of Environmental Quality*, 336: 1–17.

571 Alonso, E. E., Romero, E., Hoffmann, C. and García-Escudero, E. 2005. Expansive bentonite–sand mixtures in cyclic
572 controlled-suction drying and wetting. *Engineering Geology*, 81: 213–226.

573 Alonso, E. E., Vaunat, J. and Gens, A. 1999. Modelling the mechanical behaviour of expansive clay. *Engineering*
574 *Geology*, 54: 173–183.

575 Alshihabi, O., Shahrour, I. and Mieussens, C. 2002. Experimental study of the influence of suction and drying/wetting
576 cycles on the compressibility of a compacted soil. *Proceedings of 1st International Conference on Unsaturated Soils*,
577 Balkema, Rotterdam, The Netherlands, pp. 541–545.

578 Aubertin, M., Mbonimpa, M., Bussière, B. and Chapuis, R. 2003. A model to predict the water retention curve from
579 basic geotechnical properties. *Canadian Geotechnical Journal*, 40: 1104–1122.

580 Azizi, A. 2016. Effects of hydraulic repeated loads on the hydromechanical response of an unsaturated silty soil. PhD
581 Thesis, Politecnico di Milano.

582 Azizi, A., Jommi, C. and Musso, G. 2017. A water retention model accounting for the hysteresis induced by hydraulic
583 and mechanical wetting-drying cycles. *Computers and Geotechnics*, 87: 86-98.

584 Azizi, A., Musso, G., Jommi, C. and Cosentini, R. M. 2018. Evolving fabric and its impact on the shearing behaviour of
585 a compacted clayey silt exposed to drying-wetting cycles. *Proceedings of 7th international conference on unsaturated*
586 *soils (UNSAT2018)*, Hong Kong, pp. 641-646.

587 Bear, J. 1972. Dynamics of Fluids in Porous Materials. American Elsevier.

588 Benson, C. and Khire, M. 1995. Earthen covers for semi-arid and arid climates. *Landfill Closures*, J. Dunn and U. Singh
589 eds., ASCE, New York, 201–217.

590 Benson, C. H., Sawangsuriya, A., Trzebiatowski, B. and Albright, W. H. 2007. Postconstruction changes in the
591 hydraulic properties of water balance cover soils. *Journal of Geotechnical and Geoenvironmental Engineering*, 133(4):
592 349–359.

593 Bishop, A. 1959. The principle of effective stress. Tecnisk Ukeblad, 39: 859–863.

594 Calabresi, G., Colleselli, F., Danese, D., Giani, G. P., Mancuso, C., Montrasio, L., Nocilla, A., Pagano, L., Reali, E. and
595 Sciotti A. 2013. A research study of the hydraulic behaviour of the Po river embankments. *Canadian Geotechnical*
596 *Journal*, 50(9): 947-960.

597 Casini, F., Vaunat, J., Romero, E. and Desideri, A. 2012. Consequences on water retention properties of double-porosity
598 features in a compacted silt. *Acta Geotechnica*, 7(2): 139–150.

599 Chapuis, 2002. Full-scale hydraulic performance of soil–bentonite and compacted clay liners. *Canadian Geotechnical*
600 *Journal*, 39 (2): 417–439.

601 Croney, D. 1977. The design and performance of road pavements. London: Her Majesty's Stationery Office.

602 Cui, Y. J., Loiseau, C. and Delage, P. 2002. Microstructure changes of a confined swelling soil due to suction controlled
603 hydration. *Proceeding of 3rd Int. Conf. on Unsaturated Soils (UNSAT 2002)*, Recife, Brazil (ed. Jucá, J. F. T., de
604 Campos, T. M .P. and Marinho, F .A .M.), Lisse: Swets and Zeitlinger, Vol. 2, pp. 593-598.

605 Cuisinier, O., Auriol, J. C., Tangi, L. B. and Dimitri, D. 2011. Microstructure and hydraulic conductivity of a
606 compacted lime-treated soil. *Engineering Geology*, 123 (3): 187–193

607 Cuisinier, O. and Masrouri, F. 2005. Hydromechanical behaviour of a compacted swelling soil over a wide suction
608 range. *Engineering Geology*, 81: 204–212.

609 Daniel, D. E. 1987. Earthen liners for land disposal facilities. *Geotech. Practice for Waste Disposal*. No. 13, R. D.
610 Woods, ed., Ann Arbor, Mich., 21–39.

611 Delage P. and Lefebvre G. 1984. Study of the structure of a sensitive Champlain clay and of its evolution during
612 consolidation. *Canadian Geotechnical Journal*, 21(1): 21–35.

613 Delage, P. and Pellerin, F.M. 1984. Influence de la lyophilisation sur la structure d'une argile sensible du Québec. *Clay*
614 *Minerals*, 19: 151-160.

615 Della Vecchia, G., Dieudonne, A. C., Jommi, C. and Charlier, R. 2015. Accounting for evolving pore size distribution
616 in water retention models for compacted clays. *International Journal for Numerical and Analytical Methods in*
617 *Geomechanics*, 39 (7): 702-723.

618 Della Vecchia, G., Jommi, C. and Romero E. 2013. A fully coupled elastic–plastic hydromechanical model for
619 compacted soils accounting for clay activity. *International Journal for Numerical and Analytical Methods in*
620 *Geomechanics*, 37 (5): 503–535.

621 Drumm, E., Boles, D. and Wilson, G. 1997. Desiccation cracks result in preferential flow. *Geotech. News*, 152: 22–25.

622 Durner W. 1994. Hydraulic conductivity estimation for soils with heterogeneous pore structure. *Water Resources*
623 *Research*, 30(2): 211–223

624 Eching, S. O. and Hopmans, J. W. 1993. Optimization of Hydraulic Functions from Transient Outflow and Soil Water
625 Pressure Data. *Soil Science Society of America Journal*, Vol. 57, pp. 1167–1175.

626 Fleureau J. M., Verbrugge J. C. , Huergo P. J. , Correia A. G. , Kheirbek-Saoud S. 2002. Aspects of the behaviour of
627 compacted clayey soils on drying and wetting paths. *Canadian Geotechnical Journal,* 39: 1341–1357.

22

628 Fredlund, D. G. and Rahardjo, H. 1993. Soil Mechanics for Unsaturated Soils. John Wiley and Sons, Inc., Hoboken, NJ,
629 USA. doi: 10.1002/9780470172759.ch1.

630 Fujimaki, H. and Inoue, M. 2003. Reevaluation of the Multistep Outflow Method for Determining Unsaturated
631 Hydraulic Conductivity. *Vadose Zone Journal*, 2, pp. 409–415.

632 Gens, A. and Alonso, E. E. 1992. A framework for the behaviour of unsaturated expansive clays. *Canadian
633 Geotechnical Journal*, 29: 1013–1032.

634 Iyer, B. 1990. Pore water extraction – comparison of saturation extract and high-pressure squeezing. *Physico-chemical
635 Aspects of Soils and Related Materials – ASTM STP 1095 K.P. Hoddinot and R.O. Lamb (eds), Philadelphia,* 159-170.

636 Jommi, C. 2000. Remarks on the constitutive modelling of unsaturated soils. In *Experimental Evidence and Theoretical
637 Approaches in Unsaturated Soils*, Tarantino A, Mancuso C (eds). AA. Balkema, Rotterdam, 139–153.

638 Koliji, A., Vulliet, L. and Laloui, L. 2010. Structural characterization of unsaturated aggregated soil. *Canadian
639 Geotechnical Journal*, 47(3): 297-297.

640 Leong, E., He, L. and Rahardjo, H. 2002. Factors Affecting the Filter Paper Method for Total and Matric Suction
641 Measurements. Geotechnical Testing Journal 25(3): 322-333.

642 Lloret, A., Villar, M. V., Sanchez, M., Gens, A., Pintado, X. and Alonso, E. E. 2003. Mechanical behaviour of heavily
643 compacted bentonite under high suction changes. *Géotechnique*, 53 (1): 27–40.

644 Mašín, D. 2013. Double structure hydromechanical coupling formalism and a model for unsaturated expansive clays.
645 *Engineering Geology*, 165: 73–88.

646 Mualem, Y. 1976. A new model for predicting the hydraulic conductivity of unsaturated porous media. Water
647 Resources Research, 12(3): 513–522.

648 Musso, G., Romero, E. and Della Vecchia, G. 2013. Double-structure effects on the chemo-hydromechanical behaviour
649 of a compacted active clay, *Géotechnique*, 15: 206-220.

650 Nocilla, A., Coop, M. R. and Colleselli, F. 2006. The mechanics of an Italian silt and example of "transitional"
651 behaviour. *Géotechnique*, 56(4): 261-271.

652 Nowamooz, H. and Masrouri, F. 2009. Density-dependent hydromechanical behaviour of a compacted expansive soil.
653 *Engineering Geology*, 106: 105–115.

654 Rojas J.C, Mancuso C. and Danese D. 2010. Pre and post-construction characterization of an embankment fill material.
655 *Proceedings of the 4th Asia Pacific conference on unsaturated soils*, Newcastle, Australia, 23-25 November 2009,
656 Buzzi O. Fytus S. and Sheng D. editors, CRC press.

657 Romero, E., Gens, A. and Lloret, A. 1999. Water permeability, water retention and microstructure of unsaturated
658 compacted Boom clay. Engineering Geology, 54: 117-127.

659 Romero, E. 2013. A microstructural insight into compacted clayey soils and their hydraulic properties. *Engineering
660 Geology*, 165: 3–19.

661 Romero, E., Della Vecchia, G. and Jommi, C. 2011. An insight into the water retention properties of compacted clayey
662 soils. *Géotechnique*, 61(4): 313–328.

663 Romero, E. and Jommi, C. 2008. An insight into the role of hydraulic history on the volume changes of anisotropic
664 clayey soils. *Water Resources Research*, 44, W12412:1–W12412:16.

665 Romero, E. and Vaunat, J. 2000. Retention curves of deformable clays. proc. int. workshop on unsaturated soils. In
666 Tarantino, A. and Mancuso, C., editors, *Experimental Evidence and Theoretical Approaches in Unsaturated Soils*, 91–
667 106, Trento, Italy. AA. Balkema, Rotterdam.

668 Romero, E., Vaunat, J. and Merchan V. 2014. Suction effects on the residual shear strength of clays. *Journal of Geo-
669 Engineering Sciences* 2 (2014) 17–37. doi:10.3233/JGS-141320.

670 Rouainia, M., Davies, O., O'Brien, T. and Glendinning, S. 2009. Numerical modelling of climate effects on slope
671 stability. *Proceedings of the Institution of Civil Engineers – Engineering Sustainability*, 162(2): 81–89.

672   Sharma, R. S. (1998). Mechanical behaviour of unsaturated highly expansive clays. PhD Thesis, Oxford University.

673   Smethurst, J. A., Clark, D. and Powrie, W. 2006. Seasonal changes in pore water pressure in a grass-covered cut slope
674   in London Clay. *Géotechnique*, 56 (8): 523-537.

675   Tarantino A., De Col S. 2008. Compaction behaviour of clay. *Géotechnique*, 58 (3): 199–213.

676   U.S. Department of Agriculture (USDA) 1950. Diagnosis and improvement of saline and alkali soils, Agricultural
677   Handbook No. 60, USDA, Washington, DC.

678   van Dam, J. C., Stricker, J. N. M. and Droogers, P. 1994. Inverse Method to Determine Soil Hydraulic Functions from
679   Multistep Outflow Experiments. Soil Science Society of America Journal, Vol. 58, pp. 647– 652.

680   Van Genuchten, M. T. 1980. A closed-form equation for predicting the hydraulic conductivity of unsaturated soils. *Soil
681   Science Society of America Journal*, 44: 892–898.

682   Vassallo, R., Mancuso, C. and Vinale, F. 2007. Effects of net stress and suction history on the small strain stiffness of a
683   compacted clayey silt. *Canadian Geotechnical Journal*, 44(4): 447-462

684   Vaughan, P. R., Kovacevic, N. and Potts, D. M. 2004. Then and now: some comments on the design and analysis of
685   slopes and embankments. *Advances in Geotechnical Engineering: Proceedings of the Skempton Conference, Imperial
686   College*, London, Vol. 1, pp. 241–290.

687   Wang G., Wei X. 2015. Modeling swelling–shrinkage behavior of compacted expansive soils during wetting–drying
688   cycles. *Canadian Geotechnical Journal,* 52 (6): 783 – 79.
689
690   Wheeler, S. J., Sharma, R. S. and Buisson, M. S. R. 2003. Coupling of hydraulic hysteresis and stress-strain behaviour
691   in unsaturated soils. *Géotechnique* 53(1): 41-54.
692
693
694
695
696
697

698   **List of Tables**

705

706   **List of Figures**

710   Figure 4. Effect of repeated hydraulic loads on the water retention behaviour: (a) S_r-log(s) (b) e-log(s) (c) e_w-log(s)

711   Figure 5. (a) Changes in volumetric water content: experimental data and inverse modeling (b) Unsaturated hydraulic

712   conductivity of the as-compacted and 6D/W specimens

713   Figure 6. ESEM photomicrographs: (a) Particles, peds and macropores (b) Macropores and ped (c) Mesopores (d) Ped

714   breakage after drying-wetting cycles

715   Figure 7. Effect of repeated hydraulic loads on MIP results: (a) Evolution of pore size density function (b) Evolution of

716   intruded void ratio

717   Figure 8. Comparison between the experimental and MIP derived WRCs

718   Figure 9. Hydromechanical model proposed to reproduce the behaviour of the peds: (a) Yield surfaces in σ'_m-s plane (b)

719   Influence of plastic strains on the water retention curve

720   Figure 10. Comparing model predictions and experimental data in terms void ratio and suction: (a) Total void ratio

721   suction (b) Evolution of e_{Ma} and e_m with suction

722   Figure 11. Comparing model predictions and experimental data in terms of S_r-log(s): (a) for the as-compacted specimen

723   (b) evolution of S_{rMa} and S_{rm} during repeated hydraulic loads (c) for the 6D/W specimen

724   Figure 12. Comparing model predictions and experimental data in terms of e_w-log(s) for: (a) as-compacted specimen

725   (b) 6D/W specimen

726   Figure 13. Hydraulic conductivity predicted by the proposed model: (a) k_r-S_e (b) K_w-S_e

727

728

729

730

731

732

733

734

735
736
737
738

NOTATION

A, Activity

B, parameter of Kozeny-Carman equation

$C(s)$, moisture capacity

e, void ratio

e_{int}, intruded void ratio

e_{Ma}, macrostructural void ratio

e_{Ma0}, initial macrostructural void ratio

e_{Me}, mesostructural void ratio

e_{Mi}, microstructural void ratio

e_m, intra-peds void ratio

e_{m0}, initial intra-peds void ratio

e_w, water ratio

e_w^{sc}, water ratio in scanning domain

e_{wMa}, macrostructural water ratio

e_{wMa}^{sat}, saturated water ratio of macropores

e_{wm}, intra-peds water ratio

e_{wm}^{sat}, saturated water ratio of peds

G_s, Specific Density

h_{lC}, model parameter controls the coupled movement of LC due to SI or SD yielding

h_s, model parameter controls the coupled movement of SI and SD due to LC yielding

K_s, saturated hydraulic conductivity

K_w, hydraulic conductivity

k_r, relative permeability

k_{sc}, model parameter controlling the slope of the scanning curves

LC, loading collapse yield curve

LL, Liquid limit

n_{Ma}, m_{Ma}, α_{Ma}, parameters of van Genuchten model for macropores

n_m, m_m, α_m, parameters of van Genuchten model for intra-peds pores

$p(S_{r\text{-}int})$, intruded pressure

PI, plastic index

r, apparent pore radius

R_{Me}, threshold pore radius separating macropores from mesopores

R_{Mi}, threshold pore radius separating micropores from mesopores

RH, Relative Humidity

s, suction

s_I, suction increase yield suction

s_D, suction decrease yield suction

S_e, effective degree of saturation

S_r, degree of saturation

S_{res}, residual degree of saturation

S_{rMa}, macrostructural degree of saturation

S_{rm}, intra-peds degree of saturation

$S_{r\text{-}int}$, normalized intruded volume

T, temperature

t, time

V_s, volume of the solid phase

V_{vMa}, volume of macropores

V_{vMe}, volume of mesopores

V_{vMi}, volume of micropores

V_{vm}, intra-peds voids

V_{wMa}, volume of water within macropores

V_{wm}, volume of water within peds

w, water content

ε_v, volumetric strain

ε_m^e, elastic volumetric strain of peds

ε_m^p, plastic volumetric strains of peds

γ_w, specific weight of water

κ, model parameter controlling the slope of unloading-reloading curve for soil

κ_m, model parameter controlling the slope of unloading-reloading curve for peds

λ_m, model parameter controlling the slope of normal compression line for peds

θ, volumetric water content

ρ_d, dry density

σ_{net}, net stress

σ_v^{net}, axial net stress

σ', effective stress

σ'_{Ma}, macrostructural effective stress

σ'_m, peds effective stress

σ'^{*}_m, peds preconsolidation stress

$1/\alpha_m$, air-entry value of peds

$1/\alpha_{Ma}$, air-entry value of macropores

$1/\alpha_{m0}$, initial air-entry value of peds

$1/\alpha_{Ma0}$, initial air-entry value of macropores

Table 1. Properties of the tested soil

Variables	Value
Liquid limit LL (%)	32.6
Plastic limit PL (%)	24.3
Plasticity Index PI (%)	8.3
Activity A (-)	0.4
Specific Density G_s	2.735
Clay fraction ($d<2\mu m$, %)	20.4
$CaCO_3$ content (%)	17.3

Table 2. Properties of the as-compacted specimens

Condition	ρ_d (kg/m³)	e (-)	w (%)	S_r (-)	s (kPa)
As-compacted	1650 ± 10	0.66 ± 0.01	20 ± 0.2	0.83 ± 0.02	33

Table 3. List of hydraulic and microstructural tests carried out with reference to figures

Type of test and figure	Method	Sample type
Water retention (Fig. 5)	Axis Translation, Vapour Equilibrium	As-compacted, 3D/W, 6D/W
Saturated hydraulic conductivity (Fig. 6, Fig. 14)	Constant head	As-compacted, 1D/W, 3D/W, 6D/W
Unsaturated hydraulic conductivity (Fig. 6, Fig. 14)	Back analysis of Richard's equation	As-compacted, 6D/W
Micro-photograph (Fig. 7)	Environmental Scanning Electron Microscopy	As-compacted, 6D/W
Pore Size Distribution and Pore Size Density (Fig. 8)	Mercury Intrusion Porosimetry	As-compacted, as compacted dry, 6D/W dry, 6D/W

Table 4. Threshold pore radii and micro-structural, meso-structural and macro-structural void ratios

void ratio	Lower threshold pore radius (nm)				Void ratio			
	As-compacted	First drying	6D/W dry	6D/W wet	As-compacted	First drying	6D/W dry	6D/W wet
e_{Mi}	-	-	-	-	0.06	0.06	0.06	0.06
e_{Me}	11	11	11	11	0.36	0.35	0.32	0.32
e_{Ma}	609	609	917	917	0.24	0.23	0.25	0.28
$e=e_{Ma}+e_{Me}+e_{Mi}$	-	-	-	-	0.66	0.64	0.63	0.66

Table 5. Parameters of the water retention model

Parameters	$1/\alpha_{Ma0}$ (kPa)	n_{Ma}	m_{Ma}	$1/\alpha_{m0}$ (kPa)	n_m	m_m
Drying	64	1.75	0.83	236	2.86	0.14
Wetting	8	2.37	0.97	34	2.61	0.12

Table 6. Parameters of the mechanical model

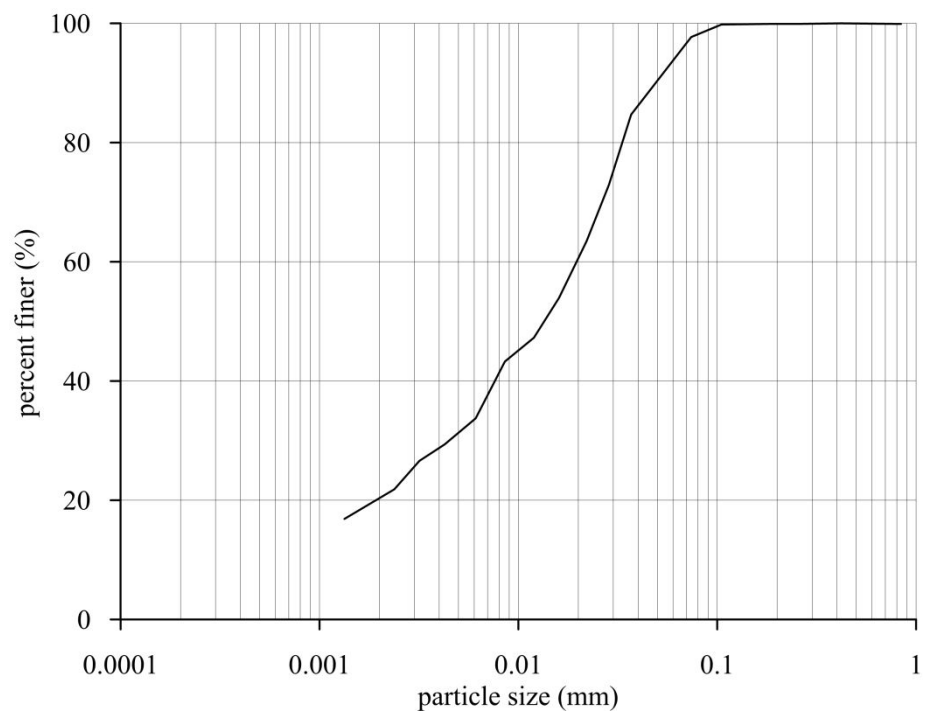| Parameters	κ	λ_m	h_{lC}	h_s	σ'^*_m kPa	s_I kPa	s_D kPa
Values	0.003	0.032	4.3	0.25	657	236	10

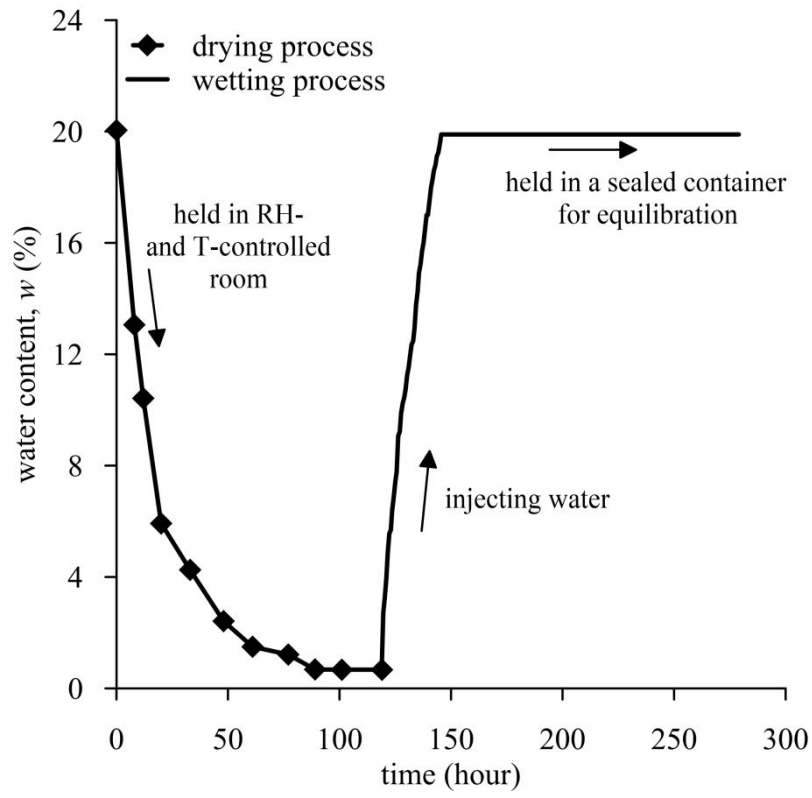Figure 1. Grain size distribution of the tested material

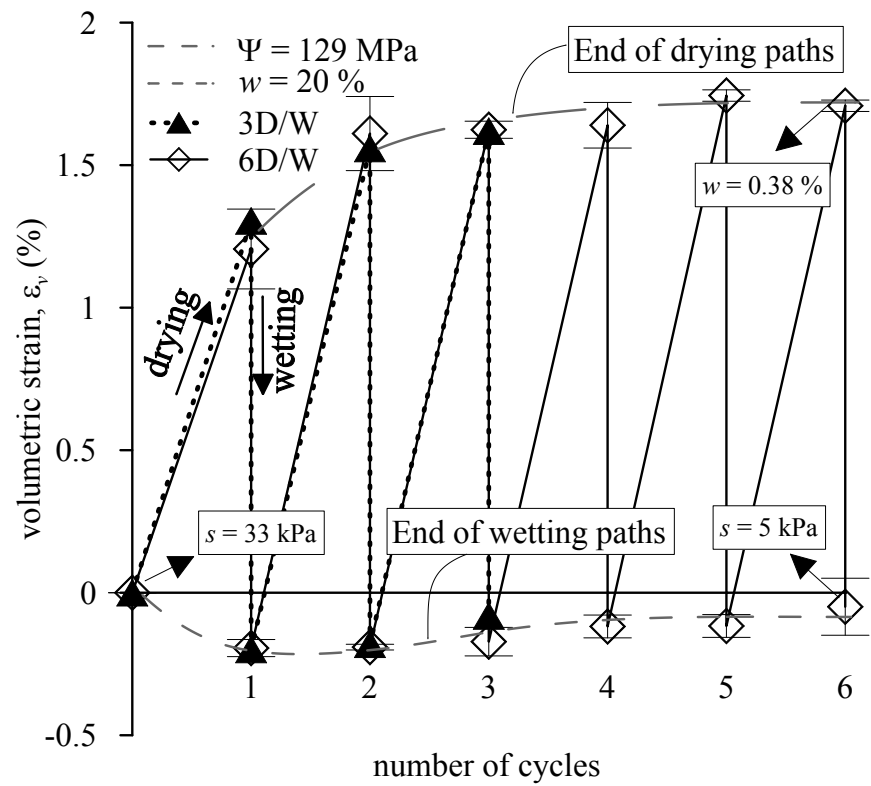Figure 2. Water content changes during drying and wetting paths

Figure 3. Mechanical response to repeated hydraulic loads: Volumetric strain with number of cycles
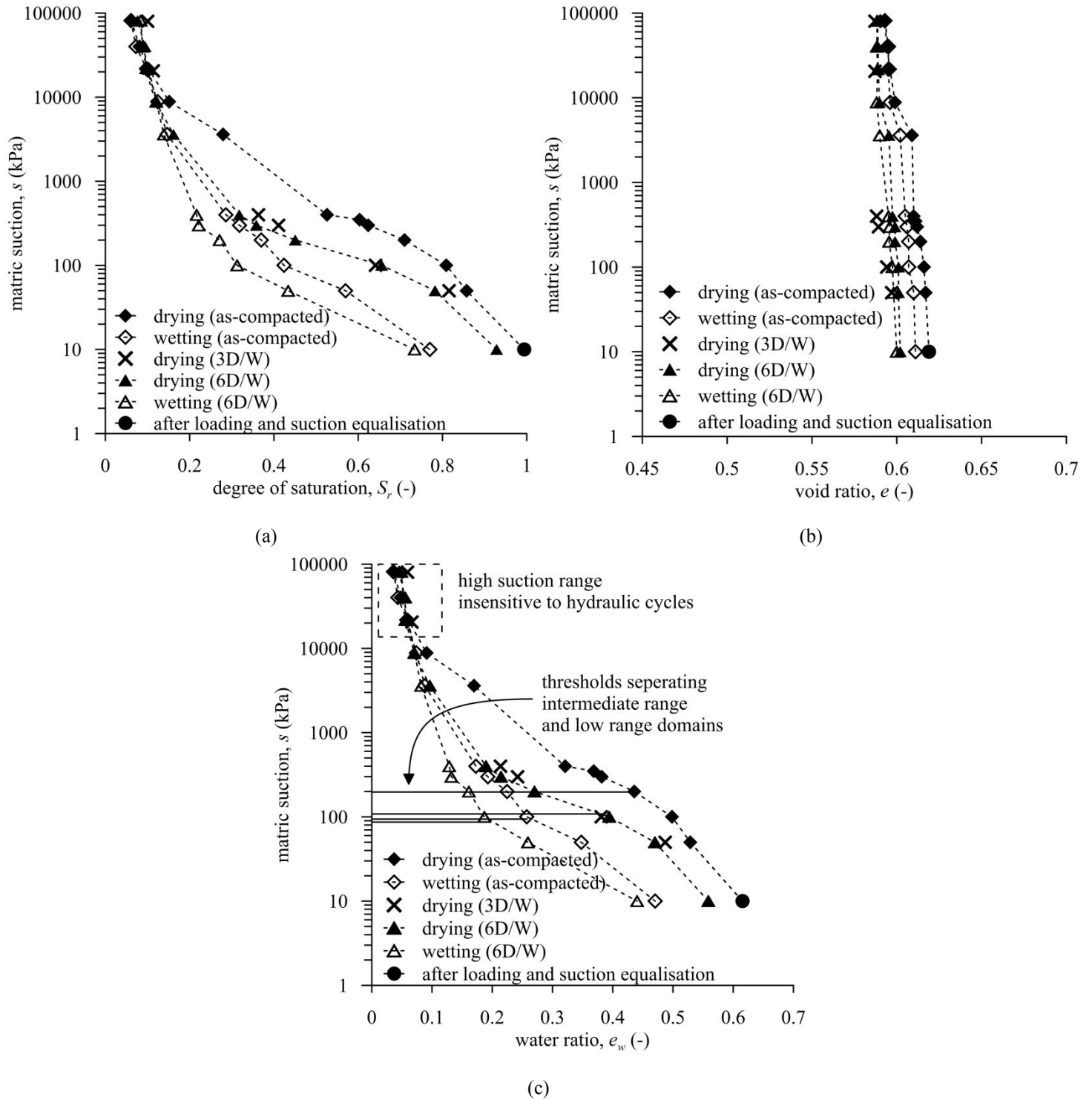
(a)

(b)

(c)

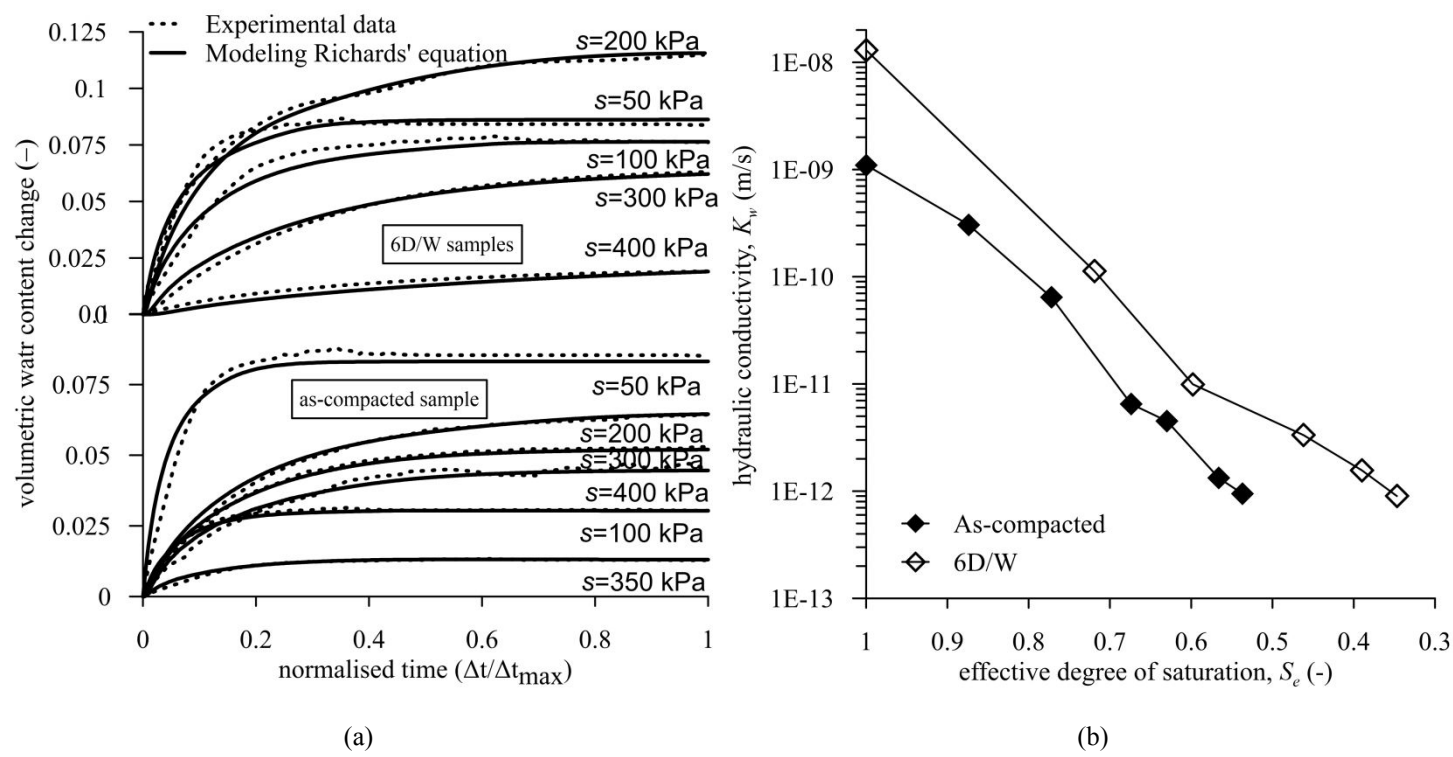Figure 4. Effect of repeated hydraulic loads on the water retention behaviour: (a) S_r-log(s) (b) e-log(s) (c) e_w-log(s)

Figure 5. (a) Changes in volumetric water content: experimental data and inverse modeling (b) Unsaturated hydraulic conductivity of the as-compacted and 6D/W specimens

(a)

(b)

(c)

(d)
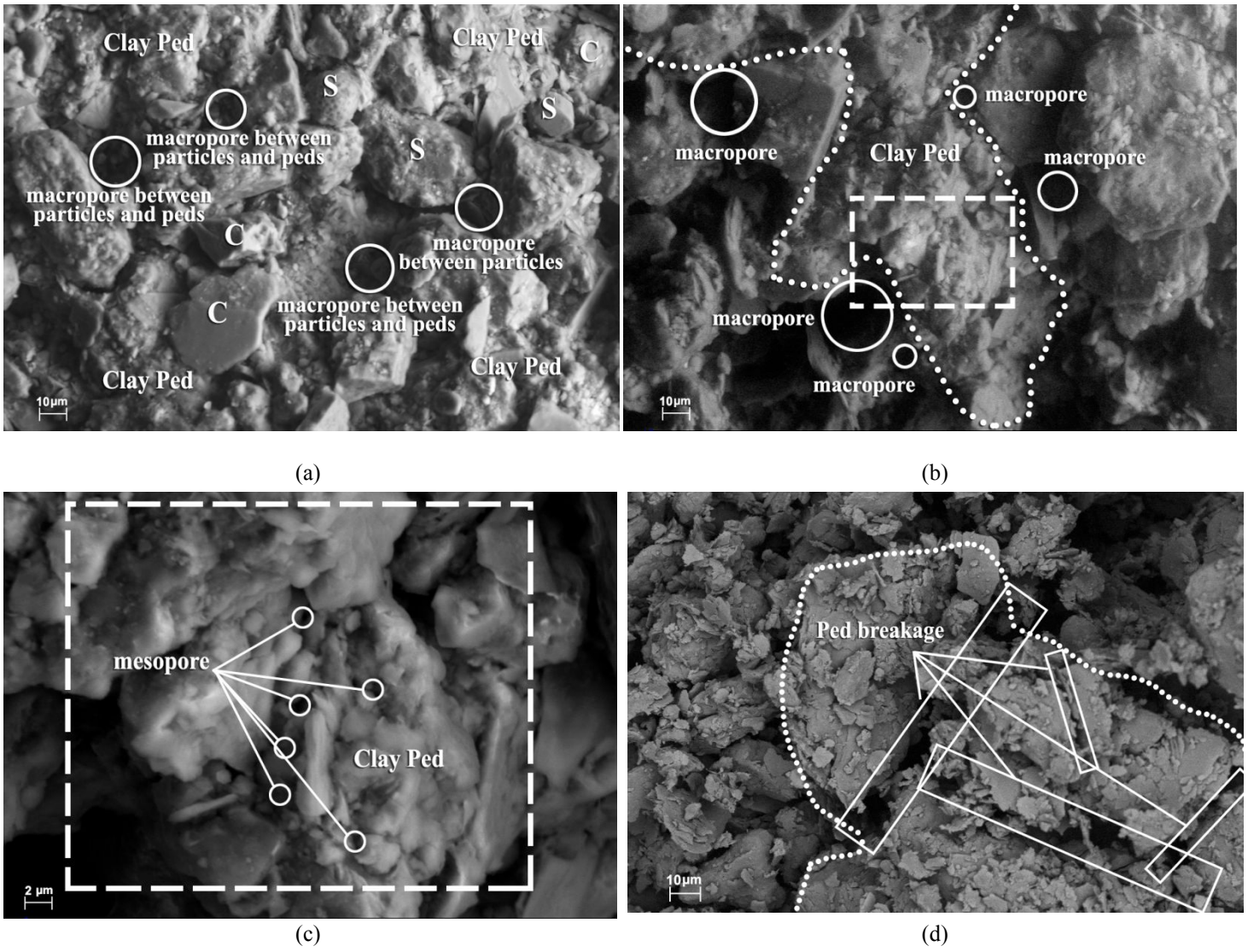
Figure 6. ESEM photomicrographs: (a) Particles, peds and macropores (b) Macropores and ped (c) Mesopores

(d) Ped breakage after drying-wetting cycles
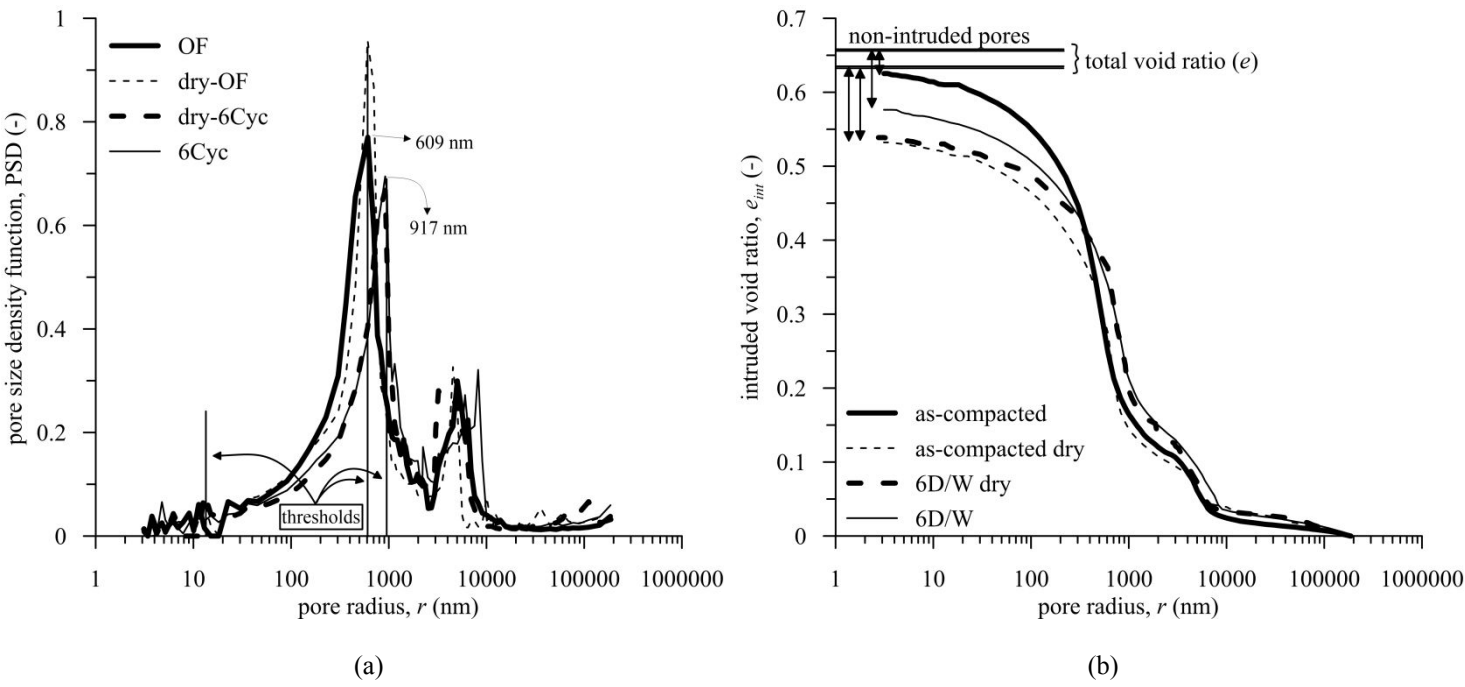
Figure 7. Effect of repeated hydraulic loads on MIP results: (a) Evolution of pore size density function (b) Evolution of intruded void

ratio
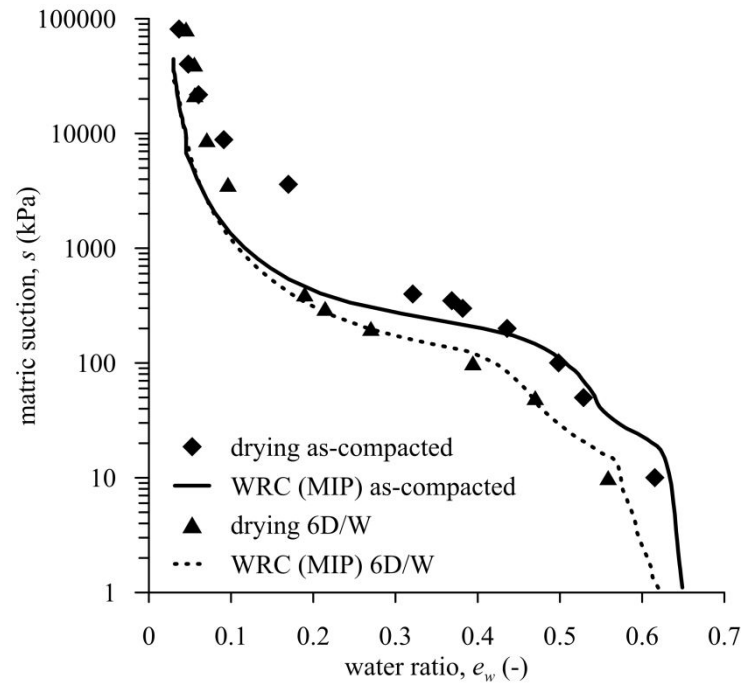
Figure 8. Comparison between the experimental and MIP derived WRCs
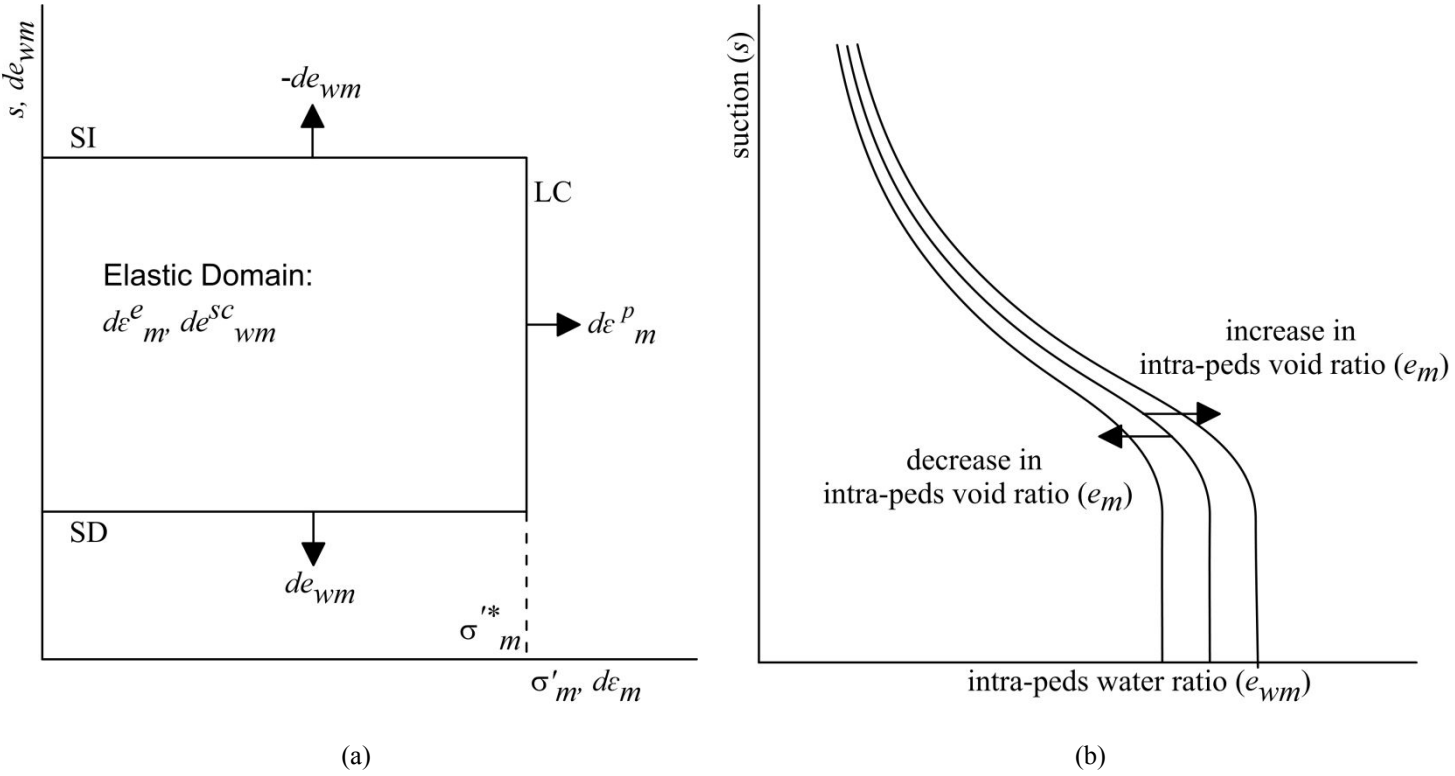
Figure 9. Hydromechanical model proposed to reproduce the behaviour of the peds: (a) Yield surfaces in σ'_m- s plane (b) Influence of

plastic strains on the water retention curve
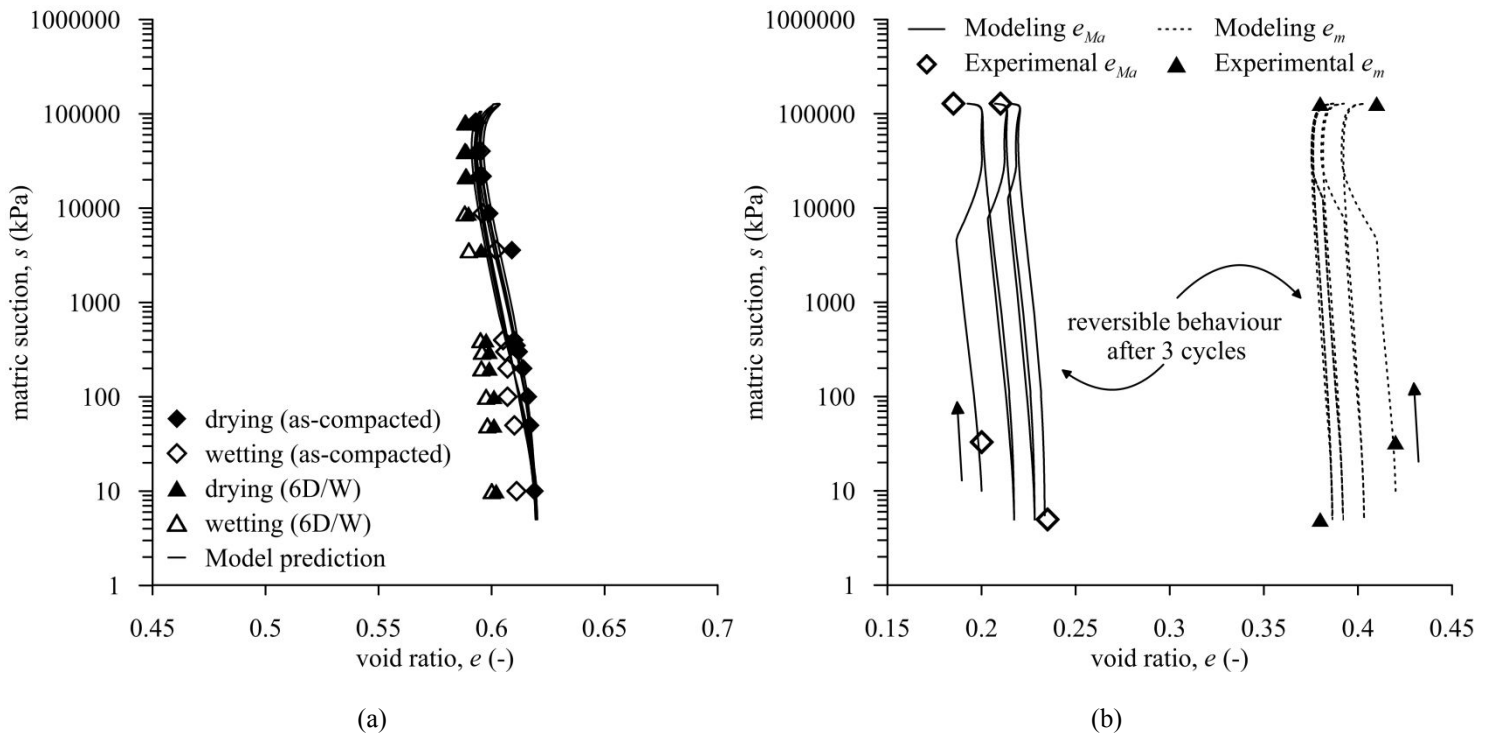
Figure 10. Comparing model predictions and experimental data in terms void ratio and suction: (a) Total void ratio suction (b)

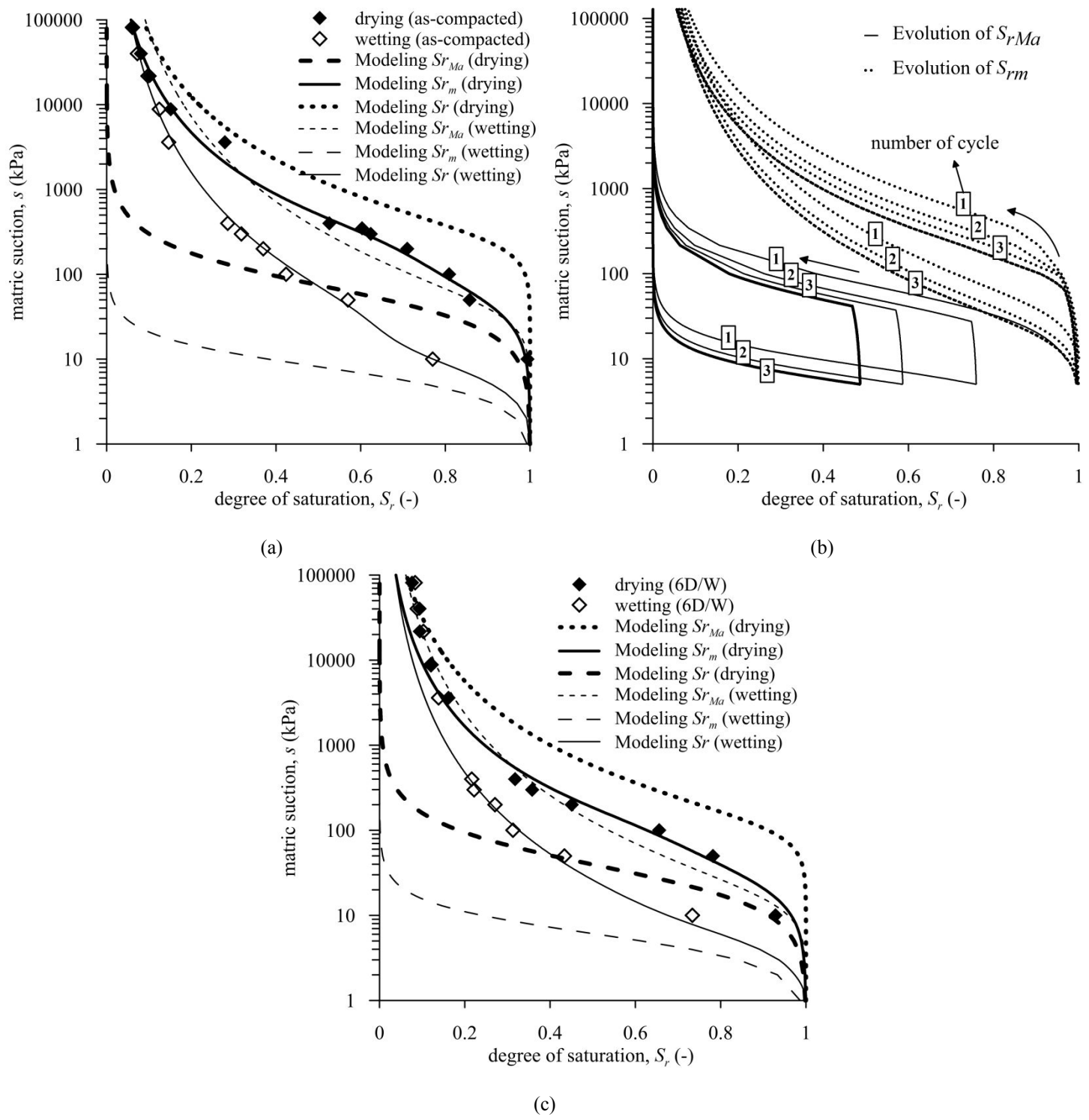Evolution of e_{Ma} and e_m with suction

(a)

(b)

(c)

Figure 11. Comparing model predictions and experimental data in terms of S_r-log(s): (a) for the as-compacted specimen (b) evolution

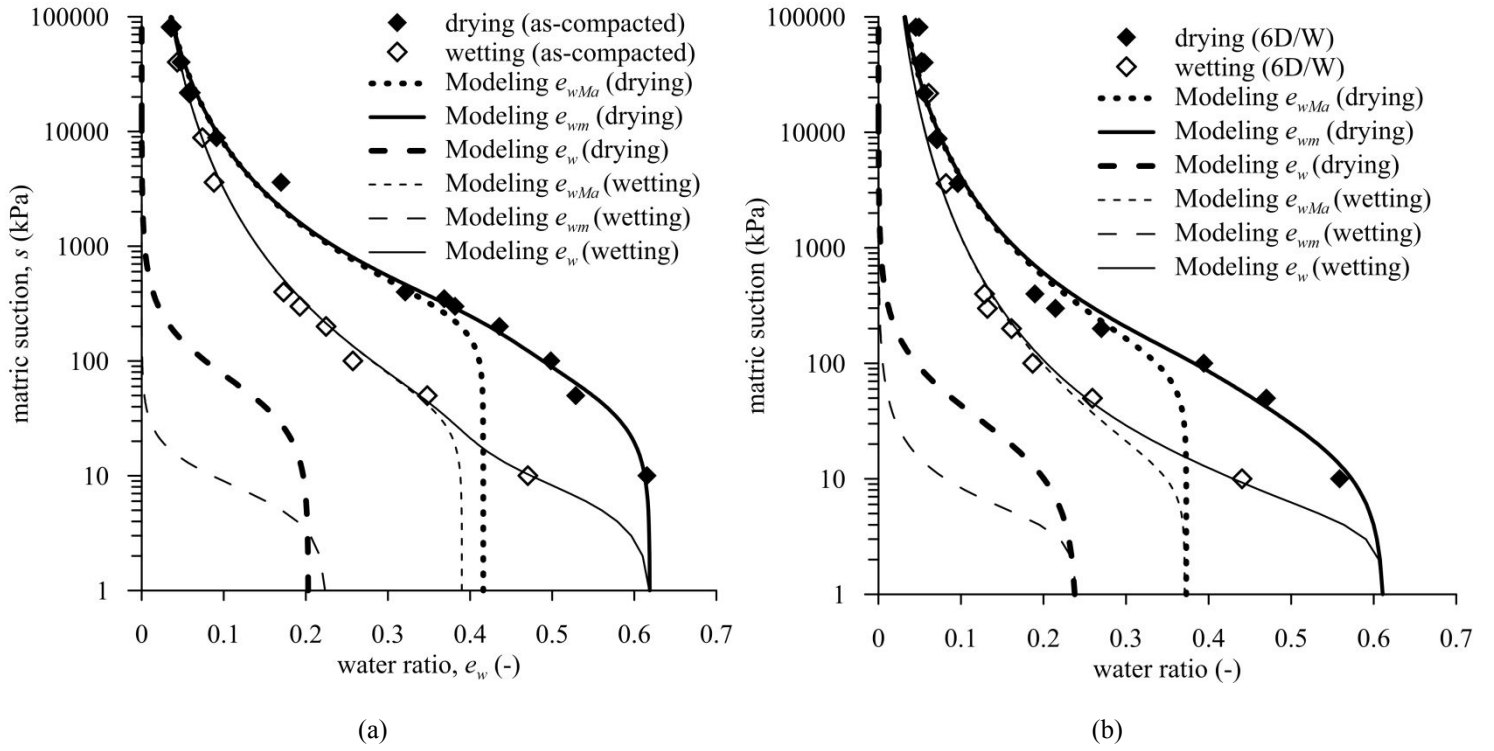of S_{rMa} and S_{rm} during repeated hydraulic loads (c) for the 6D/W specimen

Figure 12. Comparing model predictions and experimental data in terms of e_w-log(s) for: (a) as-compacted specimen (b) 6D/W
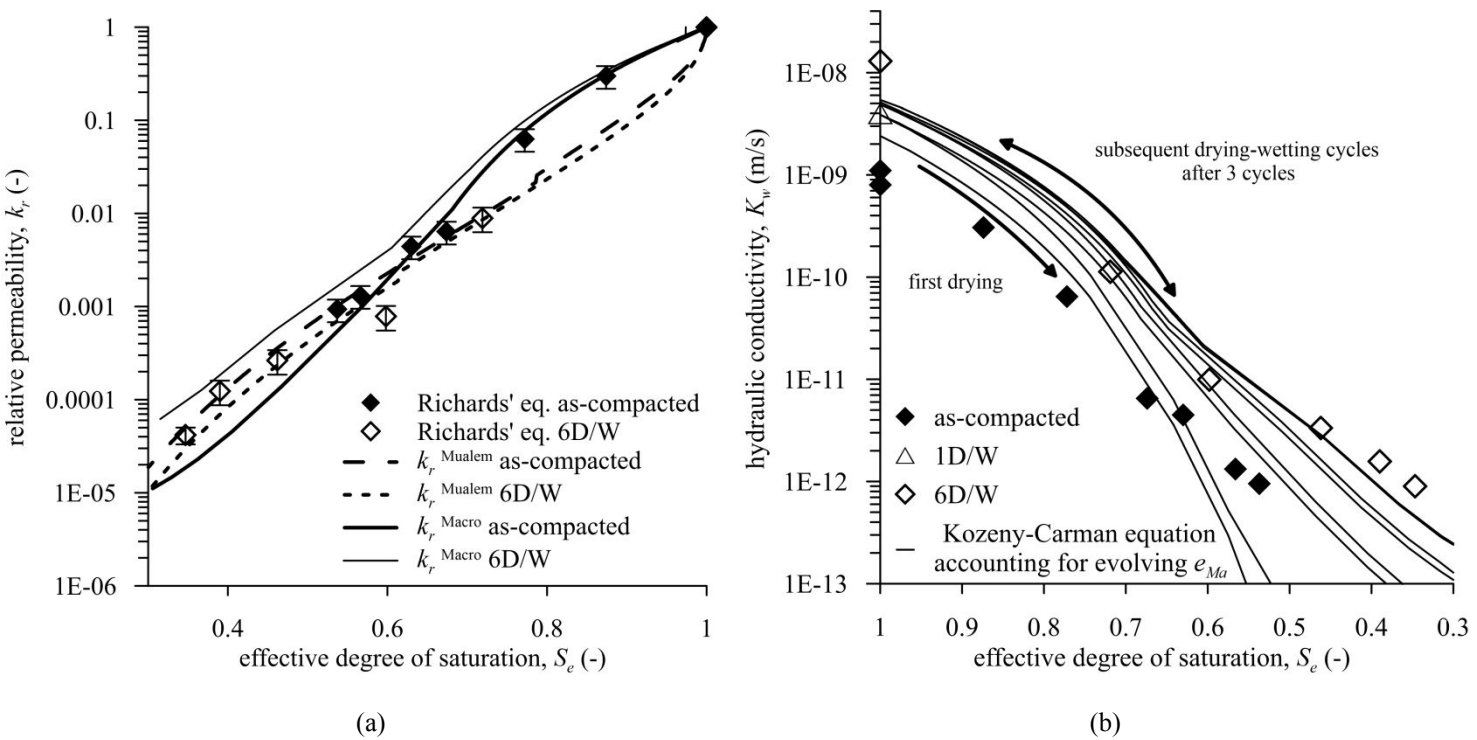
specimen

Figure 13. Permeability predicted by the proposed model: (a) k_r-S_e (b) K_w-S_e